Defining Cardiac Recovery at Single Cell Resolution

Junedh M. Amrute[1] *, Lulu Lai[2] *, Pan Ma[1], Andrew Koenig[1], Kenji Kamimoto[3,4,5], Andrea Bredemeyer[1], Thirupura S. Shankar[6], Christoph Kuppe[7,8], Farid F. Kadyrov[1], Linda J. Schulte[9], Dylan Stoutenburg[1], Benjamin Kopecky[1], Sutip Navankasattusas[6], Joe Visker[6], Samantha A. Morris[3,4,5], Rafael Kramann[7,8], Florian Leuschner[10,11], Douglas L. Mann[1], Stavros G. Drakos[6], and Kory J. Lavine[1,2,3,5,#]

Affiliations:

[1]Cardiovascular Division, Department of Medicine, Washington University School of Medicine, St. Louis, Missouri, USA.
[2]Department of Pathology and Immunology, Washington University School of Medicine, Saint Louis, Missouri, USA.
[3]Department of Developmental Biology, Washington University School of Medicine, Saint Louis, Missouri, USA.
[4]Department of Genetics, Washington University School of Medicine, Saint Louis, Missouri, USA.
[5]Center for Regenerative Medicine, Washington University School of Medicine, Saint Louis, Missouri, USA.
[6]Division of Cardiovascular Medicine & Nora Eccles Harrison Cardiovascular Research and Training Institute, University of Utah Health & School of Medicine, Salt Lake City, UT
[7]Institute of Experimental Medicine and Systems Biology and Division of Nephrology, RWTH Aachen University, Aachen, Germany
[8]Department of Internal Medicine, Erasmus Medical Center, Rotterdam, The Netherlands
[9]Division of Cardiothoracic Surgery, Department of Surgery, Washington University School of Medicine, Saint Louis, MO, 63110, USA.
[10]Department of Cardiology, University Hospital Heidelberg, Heidelberg, Germany
[11]German Centre for Cardiovascular Research (DZHK), Partner Site Heidelberg, Heidelberg, Germany

*These authors contributed equally

[#]Correspondence should be addressed to:
Kory J. Lavine, MD, PhD,
Affiliation: Division of Cardiology, Department of Medicine, Washington University School of Medicine.
Address: 660 S Euclid, Campus Box 8086, St. Louis, MO 63110.
Telephone:314-362-1171
Email: klavine@wustl.edu

Abstract

Recovery of cardiac function is the ultimate goal of heart failure therapy. Unfortunately, cardiac recovery remains a rare and poorly understood phemomenon. Herein, we performed single nucleus RNA-sequencing (snRNA-seq) from non-diseased donors and heart failure patients. By comparing patients who recovered LV systolic function following LV assist device implantation to those who did not recover and donors, we defined the cellular and transcriptional landscape and predictors of cardiac recovery. We sequenced 40 hearts and recovered 185,881 nuclei with 13 distinct cell types. Using pseudobulk differential expression analysis to detangle cell specific signatures of cardiac recovery, we observed that recovered cardiomyocytes do not revert to a normal state, and instead, retain transcriptional signatures observed in heart failure. Macrophages and fibroblasts displayed the strongest signatures of recovery. While some evidence of reversion to a normal state was observed, many heart failure associated genes remained elevated and recovery signatures were predominately indicative of a biological state that was unique from donor and heart failure conditions. Acquisition of recovery states was associated with improved LV systolic function. Pro-inflammatory macrophages and inflammatory signaling in fibroblasts were identified as negative predictors of recovery. We identified downregulation of *RUNX1* transcriptional activity in macrophages and fibroblasts as a central event associated with and predictive of cardiac recovery. *In silico* perturbation of *RUNX1* in macrophages and fibroblasts recapitulated the transcriptional state of cardiac recovery. This prediction was corroborated in a mouse model of cardiac recovery mediated by BRD4 inhibition where we observed a decrease in macrophage and fibroblast *Runx1* expression, diminished chromatin accessibility within peaks linked to the *Runx1* locus, and acquisition of recovery signatures. These findings suggest that cardiac recovery is a unique biological state and identify RUNX1 as a possible therapeutic target to facilitate cardiac recovery.

Keywords: heart failure, cardiac recovery, Runt related transcription factor 1 (RUNX1), macrophage, fibroblast, single nucleus RNA sequencing (snRNA-seq).

Introduction

Heart failure (HF) is a growing epidemic that affects over 23 million individuals worldwide and imparts a substantial burden on healthcare systems[1,2]. Restoration of cardiac function, a phenomenon referred to as cardiac recovery, represents the holy grail for heart failure therapies. Cardiac recovery is characterized by restoration of normal (or near normal) left ventricular (LV) systolic function and reversal of LV dilatation, a process termed LV reverse remodeling. Cardiac recovery is infrequently observed following initiation of goal directed medical therapy in ambulatory patients and implantation of LV assist devices (LVADs) in patients with advanced heart failure[3–6]. Individuals who experience cardiac recovery have markedly improved survival and quality of life[7,8]. At present much remains to be learned about cardiac recovery including the underlying cellular and molecular mechanisms, features that distinguish heart failure patients who will undergo recovery from those who will continue to experience disease progression, and whether cardiac recovery represents a reversion to normal or a unique biological state[9]. Unraveling the molecular basis of cardiac recovery in humans may help us identify new therapeutic targets for heart failure.

The advent of next generation sequencing has afforded researchers new opportunities to dissect the cellular diversity of human tissue across disease contexts[10,11]. Recent reports have utilize single nucleus RNA sequencing (snRNA-seq) from healthy and failing human hearts to greatly expand our understanding of human heart failure and identified cell specific transcriptional signatures in dilated and hypertrophic cardiomyopathies[12–16]. While some studies have explored mechanical unloading of the heart, there is a paucity of information regarding cardiac recovery at the single cell level. Designing and executing a study focused on cardiac recovery is challenging and must be carefully performed to discriminate cardiac recovery from mechanical unloading. To rigorously identify individuals who exhibit cardiac recovery, patients must undergo extensive phenotyping before and after LVAD implantation and paired tissue specimens need to be collected from similar regions in the LV at the time of LVAD implantation and at the time of LVAD explant.

Herein, we defined the cellular and transcriptional landscape of cardiac recovery using snRNA-seq. We compared non-diseased donor controls with heart failure patients who experienced either cardiac recovery or ongoing heart failure before and after LVAD implantation (n=40). By performing cell specific pseudobulk differential expression analysis at the patient level, we

uncovered that cardiac recovery represents a unique biological state and defined cell specific signatures of cardiac recovery that were distinct from both healthy and failing hearts. We further showed that transcriptional changes of cardiac recovery were encoded outside of the cardiomyocyte compartment predominately within macrophages and fibroblasts. We identified a *RUNX1* gene regulatory network (GRN) in macrophages and fibroblasts that was associated with and predictive of cardiac recovery using a deep neural network. *In silico* perturbation analysis[17], revealed that *RUNX1* activity in macrophages and fibroblasts was predicted to control transition of cell states towards those associated with recovery and away from those associated with heart failure. Finally, we leveraged a mouse model of cardiac recovery[18] to validate the putative role of the *Runx1* GRN in cardiac recovery. These findings uncover the biological state and cell specific mechanisms that contribute to cardiac recovery and identify *RUNX1* as a putative therapeutic target to facilitate cardiac recovery.

148 **Results**

149

150 ***Single nuclei RNA sequencing defines the cellular landscape of cardiac recovery***

151 We perform snRNA-seq on paired transmural LV specimens obtained from the apical anterior wall
152 of age- and sex-matched donor controls (n=14) and heart failure (HF) patients at the time of LVAD
153 implant and at the time of LVAD explant. HF patients were divided into those who recovered LV
154 systolic function (recovery/reverse remodeled, RR, n=5) and those demonstrated persistent
155 reduction in LV ejection fraction (mechanically unloaded, U, n=8). Echocardiograms post-LVAD
156 implant were performed using a predefined protocol where the LVAD speed was reduced to
157 assess intrinsic LV systolic function[19,20] (**Fig.1A**). After doublet removal and quality control
158 (**Extended Data Fig. 1**), we recovered 185,881 nuclei across 40 patient samples. We then
159 performed dimensional reduction, UMAP construction, and cell clustering with differential gene
160 expression to annotate cell types (**Fig. 1B**). We identified 13 transcriptionally distinct cell types
161 marked by canonical gene markers (**Fig. 1C, Extended Data Fig. 2A**). We also constructed cell
162 type specific gene set scores and detected strong separation across clusters (**Extended Data**
163 **Fig. 2B-C**). Cell composition analysis showed a drop in cardiomyocytes and increase in the
164 stromal cell fraction in HF pre- and post-LVAD samples relative to controls (**Fig. 1D, Extended**
165 **Data Fig. 2D**). Echocardiographic data revealed the maked difference in LV ejection fraction post-
166 LVAD implant between the recovered and unloaded groups (**Fig. 1E**). We then performed cell
167 type specific pseudobulk differential gene expression analysis using the following comparisons:
168 pre-LVAD HF (U-pre and RR-pre) versus donor, recovery post-LVAD (RR-post) versus pre-LVAD
169 HF, and RR-post versus donor (**Extended Data Fig. 3A-B**).

170

171 To place this DE analysis in the context of the different facets of cardiac recovery we built a Venn
172 diagram of overlapping DE genes to identify three key categories relevant to the response to heart
173 failure and cardiac recovery: (1) genes expressed specifically during recovery (recovery genes),
174 (2) genes associated with HF that were persistently changed (HF persistent genes), and (3) genes
175 associated with HF that returned to normal (HF reversed genes) (**Fig. 1F**). To identify cell types
176 which may drive cardiac remodeling, we created pairwise scatter plots of the number of
177 differentially expressed genes from the 3 comparisons (**Fig. 1G**). Within the majority of cell types,
178 HF persistent and recovery genes were found at higher frequency than HF reversed genes
179 indicating that the recovered state is not simply a reversion to normal and rather a unique
180 biological entity.

181

182 ***Cell type specific signatures of cardiac recovery***

183 To dissect which cell types display the strongest signature of recovery, we quantified the number
184 of recovery genes up- and down-regulated in each cell type. Among the major cell populations,
185 myeloid cells (monocyte, macrophages, dendritic cells) and fibroblasts had the greatest number
186 of recovery genes (**Fig. 2A-B, Extended Data Fig. 3C**). We then constructed heat maps of the
187 top 25 up- and down-regulated recovery genes in the cells types with the strongest recovery
188 signatures (myeloid, fibroblasts, endothelium, endocardium, cardiomyocytes) and observed
189 consistent and robust enrichment within the RR-post group. We observed modest enrichment of
190 the recovery signature within the U-post, suggesting that mechanical unloading may produce an
191 intermediate phenotype within the continuum of recovery (**Fig. 2C**). To assess whether the
192 transcriptional signature of recovery is unique to each cell type, we quantified the number of
193 recovery genes which overlap in more than one cell type across the five major populations and
194 found that most of the identified recovery genes are specific to a given cell type (**Fig. 2D**). Upset
195 plots were constructed to assess pairwise overlap of cardiac recovery genes among different
196 permutations of the major cell types (**Extended Data Fig. 4**). While the dominant signatures were
197 cell type specific, we found 5 up-regulated (*PTPN13, FKBP5, ZBTB16, FGD4, ZMYND8*) and 1
198 down-regulated (*CTD-3252C9.4*) recovery genes common to the five major cell types (**Fig. 2E**).
199 To ascertain whether cell type specific cardiac recovery signatures are associated with LV systolic
200 function post-LVAD implant, we performed a linear regression analysis using LV ejection fraction
201 as a surrogate for systolic function. We identified strong correlations between the ejection fraction
202 and up- and down-regulated recovery signatures (**Fig. 2F**). These findings indicate that
203 transcriptional signatures of cardiac recovery are cell type specific and are reflective of a
204 continuum of cardiac recovery.
205

206 ***Cardiomyocytes do not revert to a healthy state in cardiac recovery***

207 To dissect the recovery landscape across cell populations, we performed a pseudobulk PCA at
208 the sample level (**Extended Data Fig. 5**). We observed a strong separation between donor and
209 HF samples across most cell types. Intriguingly, for cardiomyocytes, post-U and post-RR
210 cardiomyocytes clustered with pre-LVAD HF cardiomyocytes suggesting a persistence of the HF
211 phenotype during both recovery and mechanical unloading (**Fig. 3A**). To delineate whether
212 recovery is associated with particular cardiomyocyte states, we performed high resolution
213 clustering of cardiomyocytes. We detected 5 distinct cardiomyocyte cell states with unique
214 transcriptional signatures and pathway enrichment (**Fig. 3B-E**).
215

216 Gaussian kernel density plots showed only modest shifts in cell states between pre-LVAD HF, U-
217 post, and RR-post conditions (**Fig. 3F**). We then created a pseudobulk heatmap of canonical
218 genes up- and down-regulated in HF[13,14] and found that many HF genes are persistently
219 dysregulated in recovered cardiomyocytes. Genes associated with the non-diseased donor state
220 do not return to normal levels in recovery. Of note, reduced expression of NPPA and ANKRD1
221 was observed in pre- and post-LVAD implant in patients that recovered compared to those that
222 did not recover, suggesting that the cardiomyocyte substrate may influence the propensity for
223 recovery (**Fig. 3G**). We validated key findings using *in situ hybridization*. Compared to donor
224 controls, the number of *MYH6* expressing cardiomyocytes was reduced in all pre- and post-LVAD
225 HF samples. Consistent with our psudobulk analysis, the number of *NPPA* expressing
226 cardiomyocytes was significantly increased in U-pre and U-post HF samples compared to donors.
227 Modest trends were observed in RR-pre and RR-post samples (**Fig. 3H-I**). *MYH6* and NPPA
228 expression were enriched in CM0 and CM1, respectively (**Fig. 3J**).
229
230 Using the up- and down-regulated genes in recovery from our pseudobulk analysis, we created a
231 recovery signature for cardiomyocytes that demonstrated selective enrichment in RR-post group
232 (**Fig. 3K, M**). To examine transcription factors which may modulate recovery, we used EnrichR to
233 find transcription factors predicted to regulate genes up- and down-regulated in recovery. Notably,
234 we observed up-regulation of a *GATA4* associated transcriptional network (**Fig. 3L**) and down-
235 regulation of transcription factors associated with inflammation (*STAT3*, *JUNB*, *JUND*, *NFKB1*) in
236 recovery (**Fig. 3N**). The gene signature downregulated in recovery was most enriched in the CM2
237 subset, which expressed canonical HF genes including *ANKRD1* and *NPPA* (**Extended Data Fig.
238 6A**). Among the genes down-regulated in cardiac recovery, *ABRA* was also expressed in CM2
239 and found to be reduced in HF patients that recovered pre- and post-LVAD implant (**Extended
240 Data Fig. 6B-C**). To validate that reduced cardiomyocyte *ABRA* expression is predictive of and
241 associated with cardiac recovery, we performed *in situ hybridization*. Quantification of *ABRA*
242 expressing cardiomyocytes confirmed reductions in RR-pre and RR-post compared to U-pre and
243 U-post groups (**Extended Data Fig. 6D-E**).
244
245 ***Macrophages encode signatures that associate with and predict cardiac recovery***
246 Pseudobulk PCA identified that RR-post myeloid cells clustered independent from donor or pre-
247 LVAD HF myeloid cells, indicating a strong transcriptional signature of recovery in the myeloid
248 compartment. U-post myeloid cells clustered with both RR-post and pre-LVAD myeloid cells
249 consistent with the finding that recovery transcriptional signatures identify a spectrum of recovery

250 (**Fig. 4A**). To decipher elements of cardiac recovery encoded in the monocyte, macrophage, and
251 dendritic cell compartment, we sub-clustered and identified 9 distinct cell states with unique
252 transcriptional signatures and pathway enrichment (**Fig. 4B-C, Extended Data Fig. 7A-B**). Cell
253 composition analysis showed expansion of Mac1 and Mac2 and reduction of Mac5 in the U-pre
254 and U-post groups relative to donors, RR-pre, and RR-post groups (**Fig. 4B, Extended Data Fig.
255 7D**). We next plotted the myeloid recovery signature (**Fig. 2**) in the UMAP space split by donor,
256 pre-LVAD HF, U-post, and RR-post groups and observed a strong enrichment in the RR-post
257 group and modest expression in the U-post group. The recovery signature was evident within all
258 myeloid cell clusters (**Fig. 4D**). To functionally classify the recovery signature, we performed
259 pathway analysis (EnrichR, WikiPathways database) and detected enrichment for EGF, HGF,
260 androgen receptor, oncostatin M, and glucocorticoid receptor signaling (**Extended Data Fig. 7C**).
261
262 We have previously identified a role for cardiac resident macrophages in adaptive remodeling of
263 the heart[21–23]. To assess whether cardiac resident macrophages are involved in cardiac recovery,
264 we generated RidgePlots and found that *CD163* (specific marker of cardiac resident
265 macrophages) expression was decreased pre-LVAD HF groups compared to donor controls.
266 Interestingly, *CD163* expression was restored to normal levels in the RR-post group while the U-
267 post group displayed an intermediate phenotype (**Fig. 4E**). We validated our sequencing findings
268 by performing *in situ hybridization* for *CD163* across patient groups. We observed a marked
269 reduction in the number of $CD163^+$ cells in pre-LVAD HF samples compared to donors. $CD163^+$
270 cells increased to near normal levels in the RR-post group and modestly increased in the U-post
271 group (**Fig. 4F**). To delineate whether *CD163* expression identifies a continuum of recovery, we
272 performed a linear regression analysis of LV ejection fraction versus pseudobulk *CD163*
273 expression at the patient level and found a modest correlation (R^2=0.21, p=0.03) (**Fig. 4G**).
274
275 To dissect whether certain transcription cell states of myeloid cells predict recovery prior to LVAD
276 implantation, we constructed a Gaussian kernel density plot of cell number in the pre-LVAD HF
277 group split by U-pre and RR-pre conditions (**Fig. 4H**). Intriguingly, we found that the Mac2 cluster
278 was overrepresented in the U-pre condition. Quantification of Mac2 composition across individual
279 patients confirmed expansion of this population in the U-pre relative to donor and RR-pre groups
280 (**Fig. 4I, Extended Data Fig. 7D**). Mac2 represented an inflammatory population that expressed
281 *PLAUR* and several chemokines and cytokines (**Fig. 4B, Extended Data Fig. 7A-B**). To assess
282 differences in inflammatory gene expression between U-pre and RR-pre groups, we constructed
283 and plotted an inflammation gene set score (*IL1A, IL1B, TNF, AREG, EREG, CXCL2, CXCL3,*

284 *CCL3, CCL4*) in UMAP space. The inflammatory signature was localized to the Mac2 population
285 and present selectively in the U-pre group (**Fig. 4J**), suggesting that the presence of inflammatory
286 macrophages is a negative predictor of cardiac recovery.
287
288 To decipher the origin of Mac2, we performed pseudotime analysis using Palantir in the HF
289 samples and identified three terminal monocyte-derived states: Mac2, cDC2, and Mono2 (**Fig.**
290 **4K-L**). Cell density plots showed strong phenotype shifts between each pre-LVAD and post-LVAD
291 group when viewed in a force directed layout (FDL) space (**Fig. 4L**). Consistent with the above
292 findings, we observed an enrichment for Mac2 in the U-pre group. Notably, post-LVAD
293 implantation RR-post converged towards a Mac5 phenotype while U-post displayed a divergence
294 towards Mac5 and Mac2, 4 (**Fig. 4B,L**). In particular, the RR-post group converged towards a
295 phenotype marked by enriched *CHKA* expression (**Fig. 4M**). This population largely consistented
296 of *CD163*$^{+}$ cardiac resident macrophages. We next plotted MAGIC imputed gene expression for
297 *CHKA, PLAUR,* and *RUNX1* along pseudotime within the Mac2 lineage. We observed a
298 monotonic increase in *PLAUR* and *RUNX1* expression and decreased *CHKA* expression as cell
299 differentiated towards Mac2 (**Fig. 4M**), highlighting competing differentiation trajectories between
300 heart failure and recovery.
301
302 To dissect regulatory changes that may underlie transcriptional signatures of heart failure and
303 recovery in myeloid cells, we performed TF enrichment analysis with DoRothEA[24] in the U-post
304 and RR-post groups. Transcription factors associated with inflammation (*RUNX1, NFKB1,*
305 *NFKB2, STAT3*, *ATF2, JUN*) were enriched in myeloid cells from the U-post group (**Extended**
306 **Data Fig. 7E**). Quantification of *RUNX1* expression at the patient level via pseudobulk analyses
307 revealed increased *RUNX1* expression in the donor, pre-LVAD HF, U-post groups. The
308 expression of *RUNX1* was markedly diminished in the RR-post group relative to all other groups
309 (**Fig. 4N**) – these results suggest that *RUNX1* downregulation may modulate macrophage
310 phenotype towards a unique state unlike a healthy or failing heart. We next performed a linear
311 regression for LV ejection fraction versus *RUNX1* pseudobulk expression and found a strong
312 negative correlation (R^2=0.43 and p=0.001) (**Fig. 4O**). To assess the interplay between *RUNX1*
313 and recovery we plotted a pseudobulk heatmap of *RUNX1* target genes that were differentially
314 expressed between U-pre and RR-pre groups and identified numerous pro-inflammatory
315 mediators that were enriched in the U-pre group. Collectively, these analyses highlight the
316 possibility that *RUNX1* may prevent recovery by promoting pro-inflammatory gene expression in
317 macrophages (**Extended Data Fig. 7F**).

318

319 ***Cardiac fibroblast remodeling in cardiac recovery***

320 Cardiac recovery is associated with reductions in myocardial fibrosis[25,26]. To ascertain how
321 cardiac fibroblasts shift during recovery, we first performed a pseudobulk PCA. Donor samples
322 clustered separately from the pre-LVAD and post-LVAD groups. A modest separation was also
323 observed between the RR-post group and the pre-LVAD HF groups (**Fig. 5A**). We then sub-
324 clustered the fibroblasts into 8 cell states (**Fig. 5B**) marked by distinct transcriptional signatures
325 (**Fig. 5C, Extended Fig. 8A, B)**. Cell composition and density analysis demonstrated that Fib1
326 (*SCN7A*) was enriched in donors, while Fib3 (*POSTN, THBS4, MEOX1*) and Fib7 were enriched
327 in HF (*GPC6*) (**Fig. 5D**). Pathway analysis revealed enrichment in genes associated with
328 extracellular matrix remodeling in Fib3 and actin binding in Fib7 (**Extended Data Fig. 8C**). To
329 assess whether recovered fibroblasts represent a reversion to the normal state, we generated a
330 heat map of genes enriched in donor control and HF fibroblasts at the pseudobulk level. This
331 analysis revealed the presence of both persistently dysregulated (*SVEP1, FAP, POSTN, GPX3,*
332 *APOD*) and normalized genes (*MEOX1, TGFBR3, ACSM3, PID1*) in recovered fibroblasts (**Fig.**
333 **5E**). Consistent with these findings, *in situ* hybridization for *POSTN* revealed persistence of this
334 fibroblast population during recovery (**Fig. 5O**). We then generated RidgePlots of the fibroblast
335 specific recovery signature and detected an enrichment within the RR-post group (**Fig. 5F-H**).
336 Gene ontology of the top genes upregulated in recovery suggested associations with cytoskeletal
337 organization, glucose homeostasis, and receptor tyrosine kinase signaling (**Fig. 5G**). Conversely,
338 the top pathways downregulated in recovery included TNF-a/NF-kB and TGF-beta signaling (**Fig.**
339 **5I**).

340

341 To identify cardiac fibroblast transcriptional changes that predict recovery, we performed
342 pseudobulk differential expression analysis between the RR-pre and U-pre groups. We detected
343 multiple robust differences between groups including multiple genes association with
344 inflammation (*JUNB, CXCL2, KLF2, KLF4, ISG20, FOSL2*) increased in the U-pre group (**Fig.**
345 **5J**). Pathway analysis of dysregulated genes showed strong upregulation of TNFa/NF-kB,
346 inflammatory response, TGFb, IFNg, and IL-6/STAT3 pathways (**Fig. 5K**).

347

348 To explore transcriptional programs that may drive recovery, we examined ENCODE/ChEA
349 Consensus transcription factors from the ChIP-X database and identified *RUNX1* as the most
350 downregulated transcription factor during recovery. We then plotted a heatmap of genes predicted
351 to be regulated by *RUNX1* during recovery and identified a strong downregulation in the RR-post

352 group (**Fig. 5L**). Given the above changes observed in *RUNX1* expression, predicted activity, and
353 TGF-b enrichment, we leveraged published PRO-seq data from *in vitro* fibroblasts stimulated with
354 TGF-b to assess the level of active transcription around the *RUNX1* locus. We found increased
355 RNA polymerase activity at the *RUNX1* locus following TGF-b stimulation relative to a
356 unstimulated control (**Fig. 5M**), suggesting that TGF-b signaling may regulate *RUNX1* expression
357 in cardiac fibroblasts. Next, we sought to delineate *RUNX1* expression across fibroblast cell
358 states. Density plots revealed that *RUNX1* was expressed in Fib3 along with genes known to
359 contribute to myocardial fibrosis including *POSTN, FAP,* and *MEOX1*[18,27,28]. Linear regression of
360 ejection fraction versus pseudobulk *RUNX1* expression showed a negative correlation (R^2=0.15
361 and p=0.07) (**Fig. 5N**). To explore a link between macrophage inflammatory gene expression and
362 associated *RUNX1* expression in fibroblasts, we performed a linear regression of fibroblast
363 specific *RUNX1* expression vs the macrophage inflammatory score (**Fig. 4N**) and observed a
364 correlation at the patient level (R^2=0.38 and p=0.04) (**Fig. 5P**). These results suggest that elevated
365 inflammation in macrophages in U-pre relative to RR-pre may hinder cardiac recovery by
366 modulating *RUNX1* expression in fibroblasts.
367
368 ***RUNX1 gene regulatory network is predictive of recovery***
369 To decipher the potential contribution of *RUNX1* towards promoting the recovery phenotype, we
370 performed the following analyses. First, we validated changes in *RUNX1* expression in stromal
371 cells across groups using *in situ* hybridization. Quantitation of the number of *RUNX1*$^+$ stromal
372 cells per 10x field, revealed that there were greater numbers of *RUNX1*$^+$ cells in the pre-LVAD
373 HF and U-post groups relative to donors. The RR-post group displayed reduced numbers of
374 *RUNX1*$^+$ cells relative to the pre-LVAD HF groups and was comparable to donors (**Fig. 6A-B**).
375 Next, we assessed whether *RUNX1* target gene expression is predictive of cardiac recovery using
376 deep learning. We split the pre-LVAD HF group (U-pre and RR-pre) into a training and test set,
377 built and trained a Keras classifier model, and applied the model in the test set to predict whether
378 cells from recovered samples were derived from the U-pre or RR-pre patients (**Fig. 6C**). We also
379 trained a random forest classifier as a comparator to our Keras model. We found that both the
380 Keras model and random forest classifier predicted recovery. The Keras model had a higher AUC
381 than the random forest classifier in predicting recovery (myeloid: Keras=0.945, RF=0.789 and
382 fibroblast: Keras=0.942, RF=0.836) (**Fig. 6D-E**). We then tested whether perturbation of *RUNX1*
383 could facilitate recovery in human macrophages and fibroblasts. We utilized CellOracle[17,29] to
384 build cell specific gene regulatory networks and performed an *in silico* deletion of *RUNX1*. To
385 define directional changes in cell fate resulting from *RUNX1* perturbation, we constructed a vector

386 field and visualized the data UMAP space (**Fig. 4B, Fig. 5B**). We leveraged Palantir pseudotime
387 trajectory analysis to infer the baseline flow of cells between states (**Extended Data Fig. 9A-B**).
388 To identify cell states enriched and depleted following *RUNX1* pertubation, we took the inner
389 product between control and experimental vector fields. This analysis indicated that *RUNX1*
390 perturbation in myeloid cells resulted in movement of cells away from the Mac1 and Mac2 states
391 and towards the Mac5 and monocyte states, signifying a predicted block in the differentiation of
392 inflammatory macrophages and preservation of cardiac resident macrophages (**Fig. 6F-H**).
393 *RUNX1* perturbation in fibroblasts resulted in movement of cells away from the Fib3 and Fib6
394 states and towards the Fib0, Fib2, Fib7 states, suggesting a shift away from states associated
395 with fibrosis and heart failure (**Fig. 6G-I**). These findings indicate that *RUNX1* expression is
396 reduced during recovery and predicts that downregulation of *RUNX1* activity in macrophages and
397 fibroblasts signifies the potential for recovery and drives shifts in macrophages and fibroblasts
398 away from states associated with heart failure.
399
400 To evaluate the biological plausibility of the above predictions, we leveraged published *in vivo*
401 scRNA-seq and scATAC-seq data obtained from a study investigating the potential of BRD4
402 inhibition (JQ1 treatment) to promote recovery in a mouse model of pressure overload heart
403 failure (Transverse Aortic Constriction, TAC)[18,27] (**Fig. 6J**). We re-processed the scRNA-seq data
404 and annotated major cell populations, independently clustered the scATAC-seq data, and
405 performed label transfer to annotate scATAC-seq clusters using the RNA information (**Fig. 6K**).
406 We selected the fibroblasts from the ATACseq dataset to explore changes in chromatin
407 accessibility around the *Runx1* locus with JQ1 treatment. We then performed peak to gene linkage
408 around the *Runx1* locus and identified several regions with increased accessibility in TAC relative
409 to sham fibroblasts that decreased with JQ1 treatment, and subsequently increased following
410 withdrawal of JQ1. Using publicly available BRD4 and H3K27ac ChIP-seq data from mouse left
411 ventricle we validated many of these peaks as active enhancer marks that were binding site for
412 BRD4 (**Fig. 6L**). Next, we quantified *Runx1* expression from the scRNA-seq data in macrophages
413 and fibroblasts and found that JQ1 treatment was associated with reduced *Runx1* expression
414 (**Fig. 6M**). Finally, to assess the relationship between JQ1 treatment and human signatures of
415 recovery, we examined the expression of human macrophage and fibroblast genes associated
416 with recovery across the mouse conditions. Within macrophages, the human recovery signature
417 was enriched in the JQ1 treated group and not the sham group indicating that BRD4 inhibition
418 drives the acquisition of the recovered state. The transcriptional signature of recovery was evident

419 in both sham and JQ1 treated conditions highlighting that BRD4 inhibition promotes both the
420 acquisition of the recovered state and reversion to baseline in cardiac fibroblasts (**Fig. 6N**).
421
422
423
424
425
426
427
428
429
430
431
432
433
434
435
436
437
438
439
440
441
442
443
444
445
446
447
448
449
450
451
452

453 **Discussion**

454

455 By performing snRNA-seq on donor hearts and samples from heart failure patients who either
456 recovered or did not recover LV systolic function following LVAD implantation, we defined the
457 single cell landscape of human cardiac recovery. This work elucidated that the recovered heart
458 represents a distinct biological entity rather than simply a reversion to the normal or non-failing
459 state. We discovered that the transcriptional signature of cardiac recovery is uniquely encoded
460 across cell types with dominant contributions from cardiac macrophages and fibroblasts. Pro-
461 inflammatory macrophage and fibroblast states were found to be negative predictors of recovery.
462 Construction of gene regulatory networks predicted that downregulation of RUNX1 transcriptional
463 activity in cardiac macrophages and fibroblasts as a central mechanism orchestrating cardiac
464 recovery, a possibility supported by machine learning and *in silico* transcriptional factor
465 perturbation techniques and corroborated in a mouse model of cardiac recovery mediated by
466 BRD4 inhibition These findings highlight the possibility that inhibition of RUNX1 may facilitate
467 cardiac recovery.

468

469 For patients suffering from heart failure, cardiac recovery represents the most ideal outcome.
470 Recovery of LV systolic function is observed in select individuals following the initiation of anti-
471 remodeling medications (beta adrenergic, angiotensin II and neprilysin inhibitors, aldosterone
472 antagonists) and mechanical unloading. The frequency of cardiac recovery declines with the
473 severity of heart failure. Individuals with end-stage heart failure that are eligible for LVAD
474 implantation and heart transplantation display the lowest incidence of recovery (1-2%)[3–6]. It has
475 been postulated that combined mechanical unloading and pharmacologic treatment may serve
476 as an approach to increase recovery rates in the growing advanced heart failure population where
477 treatment strategies remain limited by recipient eligibility for heart transplantation and donor organ
478 availability[30,313233]. An improved understanding of the mechanistic basis by which hemodynamic
479 changes imposed by mechanical unloading translate to molecular and structural changes
480 associated with cardiac recovery[34,35] is essential for the development of new therapeutic
481 strategies to increase the frequency of cardiac recovery. Thus, it is of the utmost clinical
482 importance to delineate the cell types and mechanisms that orchestrate acquisition and
483 maintenance of cardiac recovery.

484

485 The concept that recovery is not merely a reversion to normal is supported by both clinical and
486 biological data. Clinical trials investigating outcomes following withdrawal of anti-remodeling

487 therapy and mechanical unloading in heart failure patients who recovered LV systolic function
488 identified a significant rate of recurrent heart failure and deterioration of cardiac function. These
489 data suggest that cardiac recovery represents a state of remission and indicate that maintenance
490 of cardiac recovery requires ongoing intervention[36,37]. The possibility that the recovered heart is
491 not normal is also supported by physiological and pathological investigation demonstrating
492 abnormal contractile reserve, blunted force frequency relationship, and persistent fibrosis[4,9,38–42].
493 Consistent with our findings, bulk RNA sequencing in a mouse model of cardiac recovery
494 triggered by mechanical unloading identified a transcriptional signature that was distinct from both
495 baseline and failing conditions. While some heart failure genes normalized, the majority remained
496 persistently dysregulated and new signatures associated with recovery emerged[43]. By generating
497 a cell type specific transcriptional map of human cardiac recovery, we similarly observed that the
498 recovered human heart retains signatures of heart failure, and instead, found that recovery was
499 associated with the emergence of cell specific transcriptional states that were not found in healthy
500 or diseased conditions.
501
502 Intriguingly, we found that transcriptional signatures of cardiac recovery were predominately
503 encoded within stromal cells with the largest contribution from cardiac macrophages. Within this
504 compartment, we detected distinct contributions from monocyte-derived and cardiac resident
505 macrophages, populations with opposing functions and effects on heart failure
506 pathogenesis[21,44,45]. Patients who did not recover displayed an enrichment in monocyte-derived
507 macrophages expressing genes implicated in myocardial inflammation and heart failure (*PLAUR,*
508 *IL1B, TNF, CCL4)*[13]. The presence of this population was a negative predictor of recovery. These
509 findings are consistent with prior work identifying an association between the abundance pro-
510 inflammatory monocyte-derived macrophages that expressed CCR2 and failure to recover[44]. In
511 contrast, we observed that $CD163^+$ cardiac resident macrophages are lost in heart failure and
512 revert to normal levels in those who recover. Given that cardiac resident macrophages strongly
513 express transcriptional signatures associated with cardiac recovery and are known to possess
514 functions important for tissue healing and remodeling[23,46,47], it is likely that this population is a
515 central mediator of the recovery process.
516
517 Cardiac fibroblast activation is an important mechanism of myocardial fibrosis and heart failure
518 pathogenesis[28,48]. The exact role of fibroblasts in cardiac recovery continues to be debated. Within
519 the recovered heart, cardiac fibroblasts retained signatures of fibroblast activation including the
520 expression of *FAP, MEOX1,* and *POSTN*[13,14,18,28]. Interestingly, cardiac recovery was associated

521 with reduced expression of genes associated with inflammatory and TGF-b signaling in cardiac
522 fibroblasts, markers of immune cell driven fibroblast activation[18,49]. When viewed together with the
523 observation that pro-inflammatory macrophages persist in patients that do not recover, these
524 findings suggest that resolution of inflammatory signaling between macrophages and fibroblasts
525 may be essential for recovery. These findings are consistent with the paradigm that para-
526 inflammation leads to persistent tissue dysfunction whereas resolution of inflammation restores
527 ssue function[50].
528
529 To unravel transcriptional networks along the macrophage-fibroblast axis driving recovery, we
530 performed transcription factor enrichment and constructed gene regulatory networks associated
531 with recovery. This analysis identified downregulation of RUNX1 activity as a key feature of
532 recovery. *RUNX1* is a transcription factor with important roles in inflammatory responses and
533 hematological cancers[51,52]. Studies performed in zebrafish suggest a role in fibroblast
534 activation[53,54]. To explore a relationship between *RUNX1* in macrophages and fibroblasts in
535 cardiac recovery, we applied a deep learning approach[55,56] and found that RUNX1 target gene
536 expression measured at the time of LVAD implantation predicts acquisition of recovered versus
537 non-recovered states in both cell populations. We then used CellOracle[17] to build macrophage
538 and fibroblast specific gene regulatory networks and ascertained the predicted effects of *RUNX1*
539 deletion using *in silico* transcription factor perturbation. Within macrophages, *RUNX1* perturbation
540 resulted in predicted loss of pro-inflammatory macrophages and pathogenic fibroblasts with shifts
541 towards states observed in recovered hearts. We then tested our predictions in a clinically
542 relevant mouse model of cardiac recovery mediated by JQ1 treatment, an inhibitor of BRD4[18].
543 Using publicly available multi-omic data, we showed that BRD4 binds to the *Runx1* enhancer in
544 mouse hearts[27], suggesting that inhibition of BRD4 may disturb the *Runx1* gene regulatory
545 network. We identify enhancer peaks in fibroblasts linked to the *Runx1* gene that display
546 increased accessibility in heart failure that are diminished by JQ1 treatment, similarly to what was
547 observed at the *Meox1* locus[18]. Consistent with disruption of RUNX1 activity, JQ1 treatment led
548 to reduced *Runx1* expression in macrophages and fibroblasts. Finally, we show that JQ1
549 treatment was sufficient to trigger the emergence of the human cardiac recovery signature in
550 macrophages and fibroblasts. Collectively, these findings highlight the possibility that RUNX1
551 inhibition may serve as an approach to facilitate cardiac recovery.
552
553 Our study is not without limitations. While our sample size is limited, availability of paired (pre-
554 and post-LVAD implant) myocardial tissue specimens from patients who recover is incredibly

scarce given the low incidence of cardiac recovery and small numbers of clinical centers with robust pipelines to phenotype and capture this unique patient population. It is important to note that the *in silico* approach used to perturb *Runx1* within macrophages and fibroblasts does not consider cellular crosstalk. While an important limitation, CellOracle transcription factor perturbation studies have been validated *in vitro* and *in vivo* and used by other groups[17,29,57]. We recognize that there is no perfect mouse model to recapitulate cardiac recovery[43] and the pressure overload JQ1 mediated recovery dataset has inherent limitations. This dataset is used to test human derived hypothesis in conjunction with the human recovery data to offset this issue. Lastly, while we show *in silico* perturbation of *Runx1* is predicted to facilitate the recovery phenotype, we recognize that conditional deletion of *Runx1* in appropriate models is necessary to establish causality.

In conclusion, we provide a comprehensive single cell transcriptomic map of human cardiac recovery, establish that cardiac recovery is a biological state distinct from healthy and disease, and unravel cell type specific signatures of recovery. Furthermore, we identify shifts in macrophage and fibroblast phenotypes driven by a *RUNX1* gene regulatory network that predict the propensity for recovery. Finally, we provide orthogonal sources of evidence to suggest that disruption of *RUNX1* in macrophages and fibroblasts drives the recovered phenotype and that RUNX1 inhibition may be an effective approach to facilitate cardiac recovery.

Acknowledgments

KL is supported by the Washington University in St. Louis Rheumatic Diseases Research Resource-Based Center grant (NIH P30AR073752), the National Institutes of Health [R01 HL138466, R01 HL139714, R01 HL151078, R01 HL161185, R35 HL161185], Leducq Foundation Network (#20CVD02), Burroughs Welcome Fund (1014782), and Children's Discovery Institute of Washington University and St. Louis Children's Hospital (CH-II-2015-462, CH-II-2017-628, PM-LI-2019-829), Foundation of Barnes-Jewish Hospital (8038-88), and generous gifts from Washington University School of Medicine. JMA is supported by the American Heart Association Predoctoral Fellowship (826325). PM is supported by American Heart Association Postdoc Fellowship (916955). Figure 1A and 6C were created in BioRender.com. We thank the Genome Technology Access Center at the McDonnell Genome Institute at Washington University School of Medicine for help with genomic analysis. The Center is partially supported by NCI Cancer Center Support Grant #P30 CA91842 to the Siteman Cancer Center. This publication is solely the responsibility of the authors and does not necessarily represent the official view of NCRR or NIH.

Author Contributions

SD contributed to LVAD sample acquisition and clinical phenotyping. PM, LL, AB, and AK isolated nuclei for snRNA-seq. JA performed computational analysis. JA, KK, and SM performed GRN analysis and in silico TF perturbation analysis. JA, LL, PM, LS, DS, FK, and BK performed RNA in situ hybridization and immunohistochemistry experiments and analyzed and processed images. JA, FL, RK, DM, SD, and KL assisted in the interpretation of the data. JA constructed all figures and JA and KL drafted the manuscript. KL is responsible for all aspects of this manuscript including experimental design, data analysis, and manuscript production. All authors approved the final version of the manuscript.

Competing Interests

No disclosures.

References

1. Roger, V. L. Epidemiology of Heart Failure. *Circ. Res.* **113**, 646 (2013).
2. Jessup, M. & Brozena, S. Heart Failure. *https://doi.org/10.1056/NEJMra021498* **348**, 2007–2018 (2003).
3. Topkara, V. K. *et al.* Myocardial Recovery in Patients Receiving Contemporary Left Ventricular Assist Devices: Results from the Interagency Registry for Mechanically Assisted Circulatory Support (INTERMACS). *Circ. Heart Fail.* **9**, (2016).
4. Burkhoff, D., Topkara, V. K., Sayer, G. & Uriel, N. Reverse Remodeling With Left Ventricular Assist Devices. *Circ. Res.* **128**, 1594–1612 (2021).
5. Selzman, C. H. *et al.* Bridge to Removal: A Paradigm Shift for Left Ventricular Assist Device Therapy. *Ann. Thorac. Surg.* **99**, 360 (2015).
6. Givertz, M. M. & Mann, D. L. Epidemiology and natural history of recovery of left ventricular function in recent onset dilated cardiomyopathies. *Curr. Heart Fail. Rep.* **10**, 321–330 (2013).
7. Kanwar, M. K. *et al.* Clinical myocardial recovery in advanced heart failure with long term left ventricular assist device support. *J. Hear. Lung Transplant.* (2022). doi:10.1016/J.HEALUN.2022.05.015
8. Shepherd, C. W. & While, A. E. Cardiac rehabilitation and quality of life: a systematic review. *Int. J. Nurs. Stud.* **49**, 755–771 (2012).
9. Tseliou, E. *et al.* Biology of myocardial recovery in advanced heart failure with long-term mechanical support. *J. Hear. Lung Transplant.* (2022). doi:10.1016/J.HEALUN.2022.07.007
10. McGuire, A. L. *et al.* The road ahead in genetics and genomics. *Nat. Rev. Genet. 2020 2110* **21**, 581–596 (2020).
11. Eraslan, G. *et al.* Single-nucleus cross-tissue molecular reference maps toward understanding disease gene function. *Science (80-.).* **376**, (2022).
12. Litviňuková, M. *et al.* Cells of the adult human heart. *Nat. 2020 5887838* **588**, 466–472 (2020).
13. Koenig, A. L. *et al.* Single-cell transcriptomics reveals cell-type-specific diversification in human heart failure. *Nat. Cardiovasc. Res. 2022 13* **1**, 263–280 (2022).
14. Chaffin, M. *et al.* Single-nucleus profiling of human dilated and hypertrophic

657 cardiomyopathy. *Nature* (2022). doi:10.1038/S41586-022-04817-8
658 15. Tucker, N. R. *et al.* Transcriptional and Cellular Diversity of the Human Heart. *Circulation*
659 **142**, 466–482 (2020).
660 16. Nicin, L. *et al.* A human cell atlas of the pressure-induced hypertrophic heart. *Nat.*
661 *Cardiovasc. Res. 2022 12* **1**, 174–185 (2022).
662 17. Kamimoto, K. *et al.* Gene Regulatory Network Reconfiguration in Direct Lineage
663 Reprogramming. *bioRxiv* 2022.07.01.497374 (2022). doi:10.1101/2022.07.01.497374
664 18. Alexanian, M. *et al.* A transcriptional switch governs fibroblast activation in heart disease.
665 *Nat. 2021 5957867* **595**, 438–443 (2021).
666 19. Gupta, D. K. *et al.* Assessment of myocardial viability and left ventricular function in
667 patients supported by a left ventricular assist device. *J. Heart Lung Transplant.* **33**, 372–
668 381 (2014).
669 20. Burke, M. A. & Givertz, M. M. Assessment and management of heart failure after left
670 ventricular assist device implantation. *Circulation* **129**, 1161–1166 (2014).
671 21. Bajpai, G. *et al.* Tissue Resident CCR2- and CCR2+ Cardiac Macrophages Differentially
672 Orchestrate Monocyte Recruitment and Fate Specification Following Myocardial Injury.
673 *Circ. Res.* **124**, 263–278 (2019).
674 22. Zaman, R. *et al.* Selective loss of resident macrophage-derived insulin-like growth factor-
675 1 abolishes adaptive cardiac growth to stress. *Immunity* **54**, 2057-2071.e6 (2021).
676 23. Dick, S. A. *et al.* Self-renewing resident cardiac macrophages limit adverse remodeling
677 following myocardial infarction. *Nat. Immunol.* **20**, 29 (2019).
678 24. Garcia-Alonso, L., Holland, C. H., Ibrahim, M. M., Turei, D. & Saez-Rodriguez, J.
679 Benchmark and integration of resources for the estimation of human transcription factor
680 activities. *Genome Res.* **29**, 1363–1375 (2019).
681 25. Asleh, R., Amir, O. & Kushwaha, S. S. Dynamics of myocardial fibrosis after left
682 ventricular assist device implantation: should speeding up the scar have us scared stiff?
683 *Eur. J. Heart Fail.* **23**, 335–338 (2021).
684 26. Wilcox, J. E. *et al.* “Targeting the Heart” in Heart Failure: Myocardial Recovery in Heart
685 Failure With Reduced Ejection Fraction. *JACC Hear. Fail.* **3**, 661–669 (2015).
686 27. Stratton, M. S. *et al.* Dynamic Chromatin Targeting of BRD4 Stimulates Cardiac
687 Fibroblast Activation. *Circ. Res.* **125**, 662 (2019).
688 28. Aghajanian, H. *et al.* Targeting cardiac fibrosis with engineered T cells. *Nat. 2019*
689 *5737774* **573**, 430–433 (2019).
690 29. Bocchi, V. D. *et al.* The coding and long noncoding single-cell atlas of the developing

691 human fetal striatum. *Science (80-.).* **372**, (2021).
692 30. Rose, E. A. *et al.* Long-Term Use of a Left Ventricular Assist Device for End-Stage Heart
693 Failure. *https://doi.org/10.1056/NEJMoa012175* **345**, 1435–1443 (2001).
694 31. Miller, L., Birks, E., Guglin, M., Lamba, H. & Frazier, O. H. Use of Ventricular Assist
695 Devices and Heart Transplantation for Advanced Heart Failure. *Circ. Res.* **124**, 1658–
696 1678 (2019).
697 32. Dharmavaram, N. *et al.* National trends in heart donor usage rates: Are we efficiently
698 transplanting more hearts? *J. Am. Heart Assoc.* **10**, 19655 (2021).
699 33. Bowen, R. E. S., Graetz, T. J., Emmert, D. A. & Avidan, M. S. Statistics of heart failure
700 and mechanical circulatory support in 2020. *Ann. Transl. Med.* **8**, 827–827 (2020).
701 34. Drakos, S. G. *et al.* Bridge to Recovery: Understanding the Disconnect Between Clinical
702 and Biological Outcomes. *Circulation* **126**, 230 (2012).
703 35. Lenneman, A. J. & Birks, E. J. Treatment strategies for myocardial recovery in heart
704 failure. *Curr. Treat. Options Cardiovasc. Med.* **16**, (2014).
705 36. Halliday, B. P. *et al.* Withdrawal of pharmacological treatment for heart failure in patients
706 with recovered dilated cardiomyopathy (TRED-HF): an open-label, pilot, randomised trial.
707 *Lancet* **393**, 61–73 (2019).
708 37. Bottle, A., Faitna, P., Aylin, P. P. & Cowie, M. R. Original research: Five-year outcomes
709 following left ventricular assist device implantation in England. *Open Hear.* **8**, 1658
710 (2021).
711 38. Wang, L. *et al.* Single-cell reconstruction of the adult human heart during heart failure and
712 recovery reveals the cellular landscape underlying cardiac function. *Nat. Cell Biol. 2020*
713 *221* **22**, 108–119 (2020).
714 39. Birks, E. J. *et al.* Prospective Multicenter Study of Myocardial Recovery Using Left
715 Ventricular Assist Devices (RESTAGE-HF [Remission from Stage D Heart Failure])
716 Medium-Term and Primary End Point Results. *Circulation* **142**, 2016–2028 (2020).
717 40. Zhang, J. & Narula, J. Molecular biology of myocardial recovery. *Surg. Clin. North Am.*
718 **84**, 223–242 (2004).
719 41. Klotz, S., Jan Danser, A. H. & Burkhoff, D. Impact of left ventricular assist device (LVAD)
720 support on the cardiac reverse remodeling process. *Prog. Biophys. Mol. Biol.* **97**, 479–
721 496 (2008).
722 42. Wohlschlaeger, J. *et al.* Reverse remodeling following insertion of left ventricular assist
723 devices (LVAD): A review of the morphological and molecular changes. *Cardiovasc. Res.*
724 **68**, 376–386 (2005).

725 43. Weinheimer, C. J. *et al.* Load-Dependent Changes in Left Ventricular Structure and
726 Function in a Pathophysiologically Relevant Murine Model of Reversible Heart Failure.
727 *Circ. Heart Fail.* **11**, e004351 (2018).
728 44. Bajpai, G. *et al.* The human heart contains distinct macrophage subsets with divergent
729 origins and functions. *Nat. Med.* **24**, 1234–1245 (2018).
730 45. Epelman, S., Lavine, K. J. & Randolph, G. J. Origin and Functions of Tissue
731 Macrophages. *Immunity* **41**, 21–35 (2014).
732 46. Lavine, K. J. *et al.* Distinct macrophage lineages contribute to disparate patterns of
733 cardiac recovery and remodeling in the neonatal and adult heart. *Proc. Natl. Acad. Sci. U.*
734 *S. A.* **111**, 16029–16034 (2014).
735 47. Wong, N. R. *et al.* Resident cardiac macrophages mediate adaptive myocardial
736 remodeling. *Immunity* **54**, 2072-2088.e7 (2021).
737 48. Kuppe, C. *et al.* Decoding myofibroblast origins in human kidney fibrosis. *Nature* **589**,
738 281–286 (2021).
739 49. Khalil, H. *et al.* Fibroblast-specific TGF-β–Smad2/3 signaling underlies cardiac fibrosis. *J.*
740 *Clin. Invest.* **127**, 3770–3783 (2017).
741 50. Medzhitov, R. Origin and physiological roles of inflammation. *Nature* **454**, 428–435
742 (2008).
743 51. Sood, R., Kamikubo, Y. & Liu, P. Role of RUNX1 in hematological malignancies. *Blood*
744 **129**, 2070 (2017).
745 52. Chen, M. J., Yokomizo, T., Zeigler, B. M., Dzierzak, E. & Speck, N. A. Runx1 is required
746 for the endothelial to haematopoietic cell transition but not thereafter. *Nat. 2009 4577231*
747 **457**, 887–891 (2009).
748 53. Koth, J. *et al.* Runx1 promotes scar deposition and inhibits myocardial proliferation and
749 survival during zebrafish heart regeneration. *Development* **147**, (2020).
750 54. Hu, B. *et al.* Origin and function of activated fibroblast states during zebrafish heart
751 regeneration. *Nat. Genet. 2022* 1–11 (2022). doi:10.1038/s41588-022-01129-5
752 55. Amrute, J. M. *et al.* Cell specific peripheral immune responses predict survival in critical
753 COVID-19 patients. *Nat. Commun. 2022 131* **13**, 1–11 (2022).
754 56. Kong, Y. & Yu, T. A Deep Neural Network Model using Random Forest to Extract Feature
755 Representation for Gene Expression Data Classification. *Sci. Rep.* (2018).
756 doi:10.1038/s41598-018-34833-6
757 57. Khouri-Farah, N., Guo, Q., Morgan, K., Shin, J. & Li, J. Y. H. Integrated single-cell
758 transcriptomic and epigenetic study of cell state transition and lineage commitment in

759 embryonic mouse cerebellum. *Sci. Adv.* **8**, (2022).
760 58. Butler, A., Hoffman, P., Smibert, P., Papalexi, E. & Satija, R. Integrating single-cell
761 transcriptomic data across different conditions, technologies, and species. *Nat.*
762 *Biotechnol.* **36**, 411 (2018).
763 59. Hafemeister, C. & Satija, R. Normalization and variance stabilization of single-cell RNA-
764 seq data using regularized negative binomial regression. *Genome Biol.* **20**, 1–15 (2019).
765 60. Korsunsky, I. *et al.* Fast, sensitive and accurate integration of single-cell data with
766 Harmony. *Nat. Methods 2019 1612* **16**, 1289–1296 (2019).
767 61. Love, M. I., Huber, W. & Anders, S. Moderated estimation of fold change and dispersion
768 for RNA-seq data with DESeq2. *Genome Biol.* **15**, 1–21 (2014).
769 62. Wang, F. *et al.* RNAscope: A Novel in Situ RNA Analysis Platform for Formalin-Fixed,
770 Paraffin-Embedded Tissues. *J. Mol. Diagn.* **14**, 22 (2012).
771 63. Setty, M. *et al.* Characterization of cell fate probabilities in single-cell data with Palantir.
772 *Nat. Biotechnol. 2019 374* **37**, 451–460 (2019).
773 64. Wu, T. *et al.* clusterProfiler 4.0: A universal enrichment tool for interpreting omics data.
774 *Innov.* **2**, 100141 (2021).
775 65. Granja, J. M. *et al.* ArchR is a scalable software package for integrative single-cell
776 chromatin accessibility analysis. *Nat. Genet. 2021 533* **53**, 403–411 (2021).
777
778
779
780
781
782
783
784
785
786
787
788
789
790
791
792

Materials and Methods

Ethical Approval for Human Specimens

This study complies with all ethical regulations associated with human tissue research. Acquisition of donor samples was approved by the Washington University Institutional Review Board (study no. 201104172). All samples were procured with informed consent from patients obtained by Washington University in St Louis School of Medicine. No compensation was provided for participation. Donor and patient demographical details can be found in Supplemental Table 1. Cardiac phenotyping was performed at the time of LVAD implantation and explant and relevant cardiac function metrics are provided in Supplemental Table 2. Clinical baseline data was collected for all patients at the time of LVAD implantation and is provided in Supplemental Table 3.

Sample Selection clinical phenotyping

The recovery cohort of patients were selected to match for the following variables to the best extent: EF at the time of LVAD implant, sex, age, and clinical risk profile. Age and sex matched donors were then pulled from the Washington University in St Louis School of Medicine biobank repository. Within the LVAD cohort, patients were assigned as “reverse remodeled” or unloaded”. Donors were selected to age and sex match with the LVAD samples. RR and U samples were chosen such that EF at the time of LVAD implantation is not different between the two groups.

Human single nuclei isolation and library preparation snRNA-seq

Cardiac tissues from LVAD cores at the time of LVAD implant (U/RR-pre) and adjacent to core samples at the time of explant (U/RR-post) from paired patient were flash frozen using liquid nitrogen. Identical regions from the apex of LV from explanted donors were used. Single nuclei suspensions were generated as previously described. In brief: flash frozen sections were minced with a razor blade, transferred to a Dounce Homogenizer containing 1 mL of lysis buffer (10 mM Tris-HCl, pH 7.4, 10 mM NaCl, 3 mM $MgCl_2$ and 0.1% NP-40 in nuclease-free water) on ice. Samples were homogenized using five strokes, an additional 1 mL of lysis buffer added, and incubated on ice for 15 mins. Samples were then filtered with a 40μm filter and filter was rinsed with 1mL of lysis buffer. The mixture was then centrifuged at 500*g* for 5 min 4 °C, resuspended in

827 1mL nuclei wash buffer (2% BSA and 0.2 U μl^{-1} RNase inhibitor (Thermo Fisher, cat. no. AM2694)
828 in 1× PBS) and, filtered using a 20μm pluristrainer (Pluriselect, cat. No. SKU43-50020-03).
829 Filtered solution as centrifuged using the above criteria and resuspended in 300 µL Nuclei Wash
830 Buffer and transferred into a 5mL tube for flow cytometry. Subsequently, 1 µl DRAQ5 (5 mM
831 solution; Thermo Fisher, cat. no. 62251) was added, sample gently vortexed, and allowed to
832 incubate for 5 min prior to sorting. $DRAQ5^+$ nuclei were sorted into 300 µL Nuclei Wash Buffer
833 using a BD FACS Melody (BD Biosciences) with a 100 µM nozzle. Sorted nuclei were then
834 centrifuged using the above conditions and resuspended in Nuclei Wash Buffer for a final target
835 concentration of 1,000 nuclei/µL – nuclei were counted on a hemocytometer. Based on the nuclei
836 concentration, 10,000 target nuclei were loaded onto a Chip G for GEM generation using the
837 Chromium Single Cell 5' Reagent v1.1 kit from 10X Genomics. Reverse transcription, barcoding,
838 complementary DNA amplification and purification for library preparation were performed as per
839 the Chromium 5' v1.1 protocol at the McDonnel Genome Institute. Sequencing was performed on
840 a NovaSeq 6000 platform (Illumina) at a target read depth of 100,000 at the McDonnel Genome
841 Institute.
842
843 *Global transcriptomic map generation*
844
845 Nuclei fastq files were aligned to the whole genome pre-mRNA reference generated from the
846 GRCh38 transcriptome (with the intron flag included) using CellRanger v3 (10X Genomics).
847 Nuclei were filtered to include those with 1000 < RNA UMI count < 10,000 and mitochondrial
848 reads < 5%. After initial QC, scrublet was ran on each sample separately in Python with default
849 parameters to score nuclei and nuclei with a doublet score > 0.2 were excluded from downstream
850 analysis. We then leveraged supervised doublet removal as previously described on a per cell
851 type basis before combining all objects. Briefly, clusters were annotated into major cell
852 populations, each major cell type was subsetted, and re-normalized, PCA, UMAP embedding,
853 clustering, and DE analysis performed. Sub-clusters which did not express the gene signature of
854 the cell type or had overlapping genes across different cell types were removed. Post-
855 contamination, all cell type objects were merged to construct a cleaned object. After QC and
856 doublet removal downstream analysis was performed in Seurat v4[58]. The cleaned object was
857 normalized using SCTransform[59] with regressing out mitochondrial percent and RNA UMI counts.
858 We then computed the principal components and used these to integrate all samples with
859 harmony[60]. Informed by the ElbowPlot, we used 80 components to construct the UMAP
860 embedding, find nearest neighbors, and clustered the data at multiple resolutions. We then used

861 the FindAllMarkers function in Seurat to perform differential expression testing and annotated
862 clusters into distinct cell types based on canonical gene markers. To define cell states within each
863 major cell type, we subsetted the major cell populations, re-normalized, re-clustered, re-computed
864 the UMAP, and annotated cell states. Both the global object and each cell type object was saved
865 and used for downstream analysis and plotting in Seurat. All differential gene expression to
866 identify cell types or cell states was performed using the normalized assay with the FindAllMarkers
867 function and the Wilcoxon rank sum test with a min.pct = 0.1 and logfc.threshold = 0.25. A
868 heatmap of the top10 genes was made across cell types/states. To further substantiate our
869 annotations, we used the top genes in each cell type/state to create a gene set z-score to see
870 separation across clusters.
871
872 *Pseudobulk Differential Gene Expression*
873
874 Pseudobulk differential gene expression was performed using the DESeq2[61] package. After QC,
875 cells were subsetted for each cell type, raw counts extracted, raw counts were aggregated to the
876 sample level, data normalized using a regularized log transform, a pseudobulk PCA performed,
877 and differential expression analysis between conditions of interested via DESeq2. For pseudobulk
878 DE analysis, we made the following comparisons: (1) pre-LVAD HF (U-pre and RR-pre) vs donor,
879 (2) RR-post vs donor, and (3) RR-post vs pre-LVAD HF (U-pre and RR-pre). Genes were deemed
880 statistically significant if adjusted p-value < 0.05 and absolute(log2FC) > 0.58. Statistically
881 significant DE genes from comparisons (1) – (3) were then used to compute cardiac recovery,
882 persistent HF, and HF reversed genes within R as defined by the Venn Diagrams. Additionally,
883 we constructed UpSet plots to look at gene overlap across different cell type permutations.
884
885 *Continuum analysis with ejection fraction*
886
887 To connect transcriptional changes with patient ejection fraction within the LVAD cohort we
888 performed a simple linear regression of EF versus: (1) pseudobulk expression of genes of interest
889 in specific cell types such as CD163 and RUNX1 and (2) cell type specific pseudobulk gene set
890 score of recovery up- and down-regulated genes. Pseudobulk aggregation was done at the
891 sample level as defined above. Regressions were performed in Prism 9 (Graphpad), an R^2
892 computed for goodness of fit, and a p-value indicating whether the slope is non-zero (F-test).
893
894 *Cell composition and density shift calculations*

895

896 We used R to compute cell type composition across conditions. To assess shifts in cell density
897 within both the global object and within individual cell types, we converted the .rds object to a
898 .h5ad file format and used scanpy.tl.embedding function which employs a Gaussian kernel
899 density estimation of cell number within the UMAP embedding. Density values are scaled from 0-
900 1 within that category.

901

902 *RNAscope In Situ Hybridization*

903

904 Flash frozen LV samples were fixed for 24 hr at 4 °C in 10% neutral buffered formalin, washed in
905 1× PBS, and embedded in paraffin. Paraffin-embedded sections were cut at an 8 µm thickness
906 using a microtome. RNA In situ hybridization was performed using the RNAScope[62] Multiplex
907 Fluorescent Reagent kit v2 Assay, RNAScope 2.5 HD Detection Reagent as per the protocol –
908 RED and RNAScope 2.5 HD Duplex Assay kits (Advanced Cell Diagnostics, ACDBio) using
909 probes designed by Advanced Cell Diagnostics. Fluorescent images were collected using a Zeiss
910 LSM 700 laser scanning confocal microscope. The following RNAScope probes from ACDBio
911 were used: MYH6 (555381), NPPA (531281), CD163 (417061), POSTN (409181), PLAUR, and
912 RUNX1. Chromogenic/brightfield/fluorescent7 images were acquired using a Zeiss Axioscan Z1
913 automated slide scanner. Image processing was performed using Zen Blue and Zen Black
914 (Zeiss). Positive cells were counted using either of two approaches: (1) For fluorescent images
915 the number of positive cells counted per 10x field or (2) for chromogenic images number of
916 positive interstitial cells/total number of interstitial nuclei per 10x field. For CD163 and POSTN,
917 donor and DCM samples were used from our previously published study and re-quantified as per
918 the above approach to ensure comparability.

919

920 *Pseudotime analysis*

921

922 Palantir[63] was used to perform pseudotime analysis. To dissect monocyte fate specification in HF
923 and cardiac recovery we subsetted the myeloid object to include U-pre, U-post, RR-pre, and RR-
924 post and excluded the proliferating cells. The normalized count matrix was then exported as a .txt
925 file and loaded into Python. Palantir was then used to compute a PCA, diffusion map, and a
926 multiscale low dimensional embedding computer with 5 eigenvectors. A force directed layout was
927 then computed for visualization of trajectories and MAGIC was used to impute data for
928 visualization. The Palantir simulation was executed with classical monocytes as the starting state,

929 no terminal states specified, and 600 waypoints used. Generalized Additive Models within Palantir
930 was then sued to compute gene expression trends along the Mac2 lineage using the
931 plot_gene_trend_heatmaps function. Pseudotime, entropy, and FDL embedding values were
932 exported and subsequent plotting for visualization was performed in R/Seurat.
933
934 *Pathway Analysis and transcription factor enrichment*
935
936 Statistically significant DE cardiac recovery genes as defined above from the pseudobulk section
937 were used to perform pathway enrichment analysis. EnrichR (https://maayanlab.cloud/Enrichr/)
938 was used for pathway analysis. TF enrichment analysis was performed using DoRothEA or the
939 ENCODE and ChEA Consensus TFs from ChIP-X in EnrichR. Pathway and TF enrichment values
940 were downloaded as .csv files and plots generated in Prism. GO enrichment analysis to compare
941 cell states was done in R using clusterProlifer[64] compareClusters function using only statistically
942 significant marker genes.
943
944 *Deep Learning to Predict Recovery*
945
946 In the macrophages and fibroblasts, we exported the log-normalized and scaled counts matrix for
947 the pre-LVAD HF group (U-pre/RR-pre). The counts matrix was filtered to only include *RUNX1*
948 target genes. The target genes were obtained from low and high throughput functional studies
949 (https://maayanlab.cloud/Harmonizome/gene_set/RUNX1/CHEA+Transcription+Factor+Targets
950). Next, we used the sklearn.model_selection function to split our data into a train and test set
951 (with test.size = 0.3). We then used the StandardScaler function from the sklearn library to scale
952 the train and test feature matrices. We used Keras from tensorflow with a dropout l2 regularization
953 to train a deep neural network to classify nuclei into RR or U category. The model was compiled
954 using a 'adam' optimizer and a binary cross-entropy loss function. AUC metrics were calculated.
955 To provide an alternative comparison, we also trained. A random forest classifier using the
956 RandomForestClassifier function from the sklearn.ensemble library. Both models were applied on
957 the test dataset and ROC curves plotted to compare the two approaches. Deep learning was
958 repeated several times and the accuracy metrics were consistent across simulation runs; in each
959 run a different permutation of train/test was used.
960
961 *Gene Regulatory Network Construction*
962

963 CellOracle (v0.10.5)[17] was used to perform GRN analysis in macrophages and fibroblasts
964 separately. Processed data was imported into scanpy as .h5ad files. The dataset was then down
965 sampled to 20k nuclei to limit computational memory usage. Highly variable genes (3,000) were
966 kept for GRN construction. A promoter DNA sequences base GRN was initialized for humans.
967 Unscaled counts were used to generate the CellOracle object and KNN imputation was
968 performed. Cluster specific GRN was then constructed and the processed GRN was saved for
969 subsequent TF KO analysis.
970
971 *In Silico TF Perturbation*
972
973 For *in silico RUNX1* KO simulation in macrophages and fibroblasts the processed oracle object
974 and inferred GRNs were loaded. The GRN was then fit using ridge regression models for the
975 simulation. To simulate a KO, the *RUNX1* expression was set to 0, Next, we calculated cell state
976 transition probabilities which are visualized as vectors on a digitized grid. To establish a baseline
977 developmental flow field, we use Palantir as described before to calculate pseudotime values.
978 Next, the Gradient_calculator function from the CellOracle library was used to calculate a
979 developmental vector field on the digitized grid. As described in CellOracle, an inner product was
980 calculated between the baseline vector field and the post-KO simulation vector field to assess
981 perturbations in different cell states to understand which populations are enriched and depleted
982 post *RUNX1* KO. All visualization parameters were used as per CellOracle recommendations.
983
984 *External In Vivo Dataset Analysis*
985
986 scRNA-seq analysis: We use publicly available data with annotations from the original manuscript.
987 Specifically, we extracted the fibroblasts (POSTN+ and POSTN-) and myeloid cells. Using the
988 human pseudobulk cardiac recovery genes, we calculated a gene signature for these genes in
989 the mouse dataset and compared sham, TAC, TAC + JQ1, and TAC + JQ1 withdrawn. For the
990 purposes of reference mapping, we extracted the raw filtered matrices for all samples, processed
991 the data using the same pipeline we applied for the human data, and build a single cell map which
992 we annotated using canonical gene markers. This object was then used to annotate the ATAC-
993 seq data.
994
995 scATAC-seq analysis: Raw fragment files were used to construct arrow files in ArchR[65]. Briefly,
996 we used ArchR to calculate doublet scores, filtered doublets, only kept cells with TSS > 10, and

997 number of unique fragments > 10,000. Next, we computed an iterative LSI, integrated data with
998 harmony across samples, added clusters, and computed a UMAP embedding. To annotate cells
999 from the ATAC-seq data, we used the addGeneIntegrationMatrix function with the above
1000 processed and annotated scRNA-seq reference. Using these cluster annotations, we made
1001 pseudobulk replicates with the addGroupCoverages function. Then we used the
1002 addReproduciblePeakSet function and macs2 to call peaks. We then subsetted the fibroblasts
1003 and used ArchR to compute peak-to-gene links and used browser plots to visualize peak to gene
1004 links around the *Runx1* locus. We split the browser track by condition to assess chromatin
1005 accessibility with peaks linked to the *Runx1* gene. Within this same locus, we also leveraged
1006 publicly available BRD4 and H3K27ac ChIP-seq data[18] - .bed files were downloaded, and tracts
1007 plotted using IGV (v2.13.1).
1008
1009 *Statistics and Reproducibility*
1010
1011 Statistical significance was calculated in Prism 9 (Graphpad). For RNAscope image quantification
1012 5 fields were quantified per patient in areas of maximal staining and representative images from
1013 those areas shown in the Fig. 3, 4, 5, and 6 and Extended Data Fig. 6, 7, and 8.
1014
1015 **Data Availability**
1016
1017 Raw sequencing files can be found on the Gene Expression Omnibus (). Processed data will be
1018 made available in a user-friendly format online.
1019
1020 **Code Availability**
1021
1022 All scripts used for analysis in this manuscript can be found on GitHub ().
1023
1024
1025

Figure 1

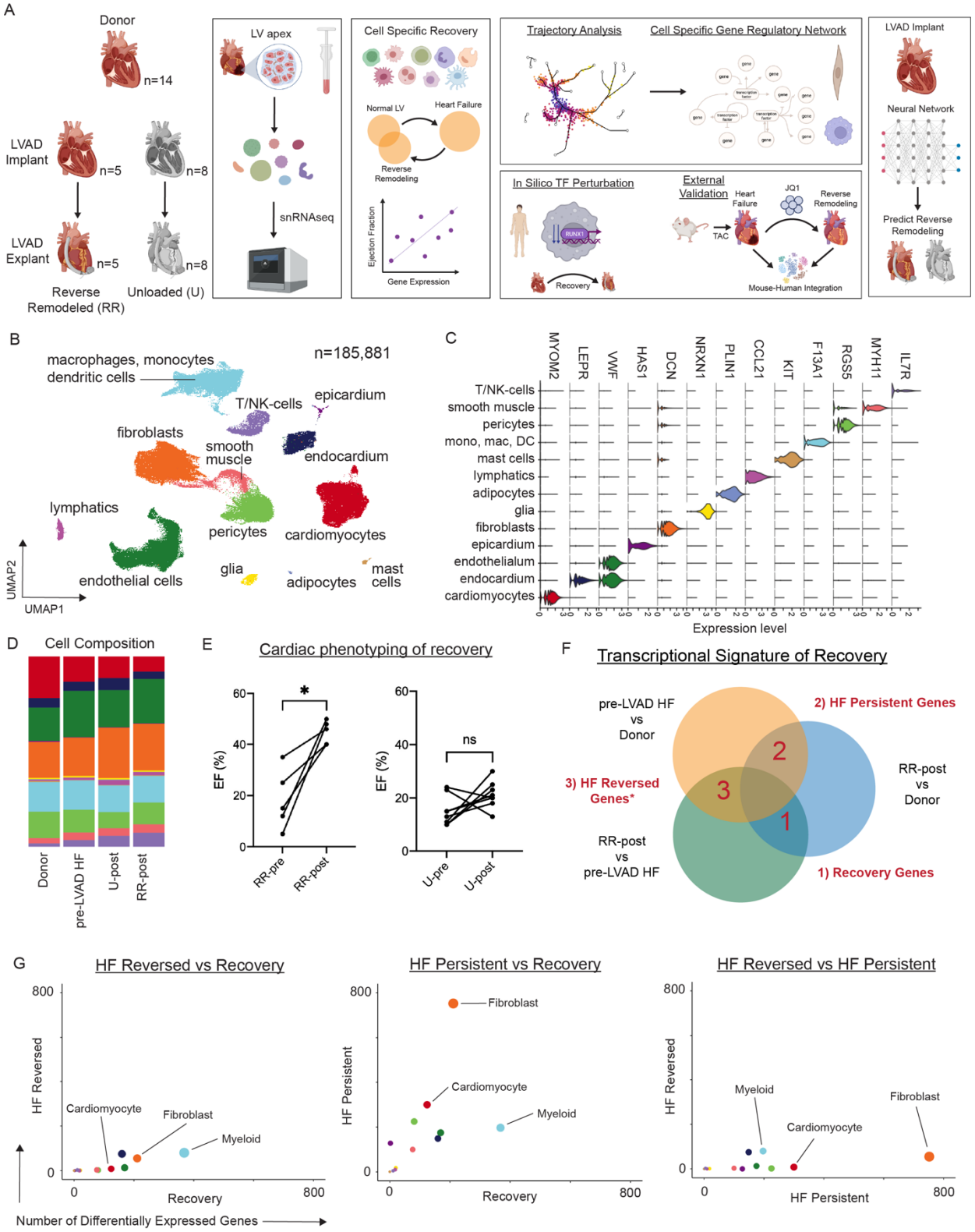
A
Donor
n=14
LVAD Implant
n=5
n=8
LVAD Explant
n=5
n=8
Reverse Remodeled (RR)
Unloaded (U)
LV apex
snRNAseq
Cell Specific Recovery
Normal LV
Heart Failure
Reverse Remodeling
Ejection Fraction
Gene Expression
Trajectory Analysis
Cell Specific Gene Regulatory Network
In Silico TF Perturbation
RUNX1
Recovery
External Validation
Heart Failure
JQ1
Reverse Remodeling
TAC
Mouse-Human Integration
LVAD Implant
Neural Network
Predict Reverse Remodeling
B
n=185,881
macrophages, monocytes
dendritic cells
T/NK-cells
epicardium
fibroblasts
smooth muscle
endocardium
lymphatics
pericytes
cardiomyocytes
endothelial cells
glia
adipocytes
mast cells
UMAP2
UMAP1
C
MYOM2
LEPR
VWF
HAS1
DCN
NRXN1
PLIN1
CCL21
KIT
F13A1
RGS5
MYH11
IL7R
T/NK-cells
smooth muscle
pericytes
mono, mac, DC
mast cells
lymphatics
adipocytes
glia
fibroblasts
epicardium
endothelialum
endocardium
cardiomyocytes
Expression level
D
Cell Composition
Donor
pre-LVAD HF
U-post
RR-post
E
Cardiac phenotyping of recovery
EF (%)
RR-pre
RR-post
ns
U-pre
U-post
F
Transcriptional Signature of Recovery
pre-LVAD HF vs Donor
2) HF Persistent Genes
3) HF Reversed Genes*
RR-post vs Donor
RR-post vs pre-LVAD HF
1) Recovery Genes
G
HF Reversed vs Recovery
HF Persistent vs Recovery
HF Reversed vs HF Persistent
HF Reversed
HF Persistent
Recovery
Cardiomyocyte
Fibroblast
Myeloid
Number of Differentially Expressed Genes

1028 **Figure 1.** Study design, global clustering, and differential expression analysis of cardiac
1029 remodeling post-LVAD implantation. (A) Study design. (B) Integrated UMAP embedding plot of
1030 snRNA-seq data across n = 40 samples and 185,881 nuclei. (C) Violin plot for canonical marker
1031 genes for cell types. (D) Cell cluster composition across conditions colored by cell type (right). (E)
1032 Paired ejection fraction measured pre- and post-LVAD implantation split by RR (left) and U (right).
1033 Paired two-tailed t-test where *P = 0.0134 (RR) and nsP = 0.1169 (U). (F) Pseudobulk differential
1034 gene expression comparisons in cardiac remodeling post-LVAD implantation categories. (G)
1035 Number of statistically significant differentially expressed genes (p-adjusted value < 0.05 with and
1036 log2 fold-change > 0.58 from DEseq2) from (F) in each cell type as pairwise comparisons where
1037 size of dot refers to the sum of axis colored by cell type.
1038
1039
1040
1041
1042
1043
1044
1045
1046
1047
1048
1049
1050
1051
1052
1053
1054
1055
1056
1057
1058
1059
1060
1061

Figure 2

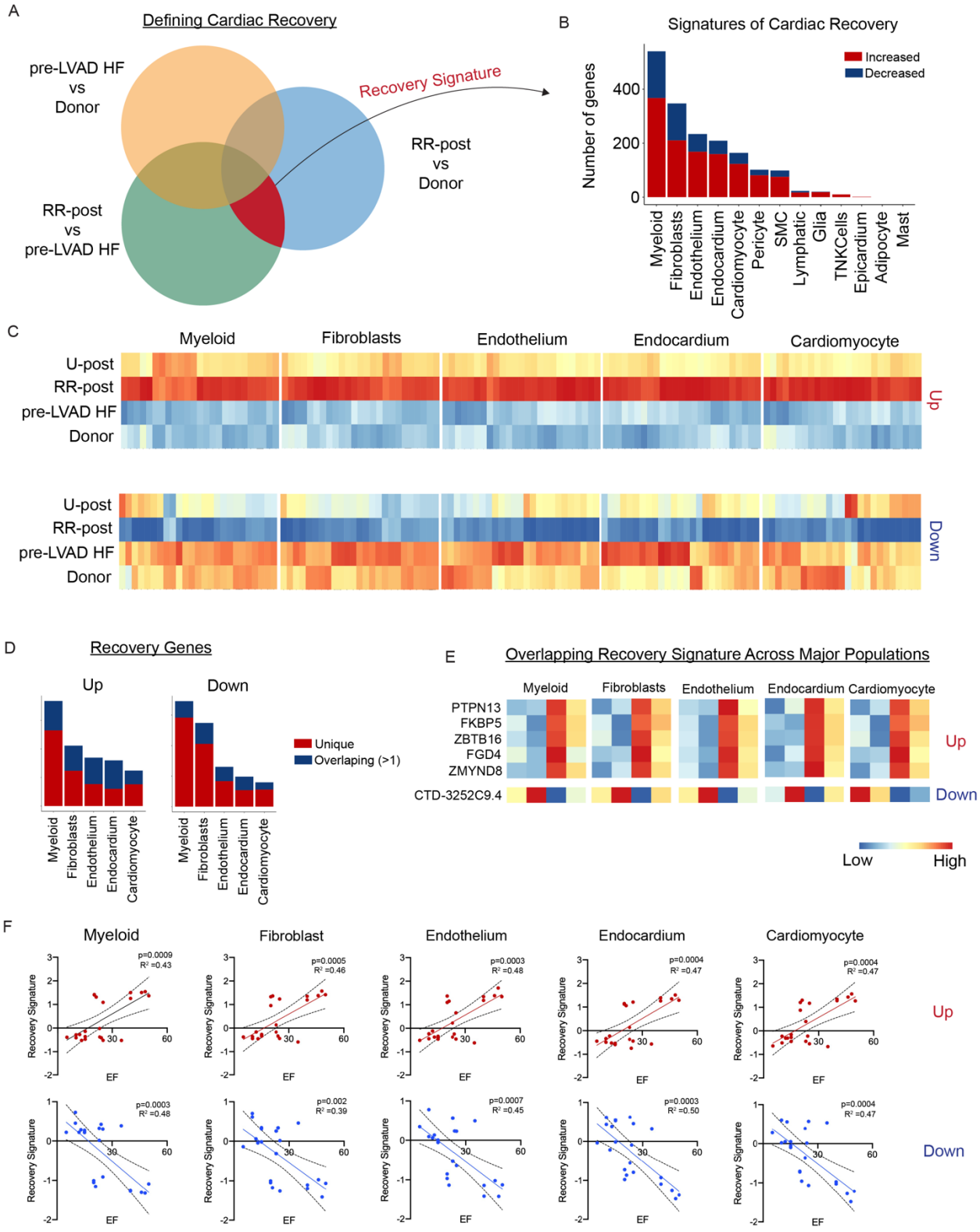
A
Defining Cardiac Recovery
pre-LVAD HF
vs
Donor
Recovery Signature
RR-post
vs
Donor
RR-post
vs
pre-LVAD HF
B
Signatures of Cardiac Recovery
Increased
Decreased
Number of genes
400
200
0
Myeloid
Fibroblasts
Endothelium
Endocardium
Cardiomyocyte
Pericyte
SMC
Lymphatic
Glia
TNKCells
Epicardium
Adipocyte
Mast
C
Myeloid
Fibroblasts
Endothelium
Endocardium
Cardiomyocyte
U-post
RR-post
pre-LVAD HF
Donor
Up
Down
D
Recovery Genes
Up
Down
Unique
Overlaping (>1)
Myeloid
Fibroblasts
Endothelium
Endocardium
Cardiomyocyte
E
Overlapping Recovery Signature Across Major Populations
PTPN13
FKBP5
ZBTB16
FGD4
ZMYND8
CTD-3252C9.4
Low
High
F
Myeloid
Fibroblast
Endothelium
Endocardium
Cardiomyocyte
Recovery Signature
EF
p=0.0009
R² =0.43
p=0.0005
R² =0.46
p=0.0003
R² =0.48
p=0.0004
R² =0.47
p=0.0004
R² =0.47
p=0.0003
R² =0.48
p=0.002
R² =0.39
p=0.0007
R² =0.45
p=0.0003
R² =0.50
p=0.0004
R² =0.47

1064 **Figure 2.** Cell type specific cardiac recovery. (A) Schematic of gene set from DE analysis which
1065 marks cardiac recovery. (B) Number of statistically significant (p-adjusted value < 0.05 with and
1066 log2 fold-change > 0.58 from DESeq2) genes from pseudobulk DE analysis which are up- and
1067 down-regulated in cardiac recovery across cell types. (C) Pseudobulk heatmaps of top genes up-
1068 (top) and down-regulated (bottom) in cardiac recovery in major cell populations split by donor, HF
1069 pre-LVAD, reverse remodeled, and unloaded. (D) Number of unique and overlapping cardiac
1070 recovery genes in major cell populations. (E) Pseudobulk expression of cardiac recovery genes
1071 which overlap among the major cell populations. (F) Polygenic recovery score of up- and down-
1072 regulated genes in cardiac recovery versus patient EF as a simple linear regression. Dotted line
1073 indicates 95% confidence interval, R^2 goodness of fit, and p-value indicating whether the slope is
1074 significantly non-zero using an F test.
1075
1076
1077
1078
1079
1080
1081
1082
1083
1084
1085
1086
1087
1088
1089
1090
1091
1092
1093
1094
1095
1096
1097

Figure 3

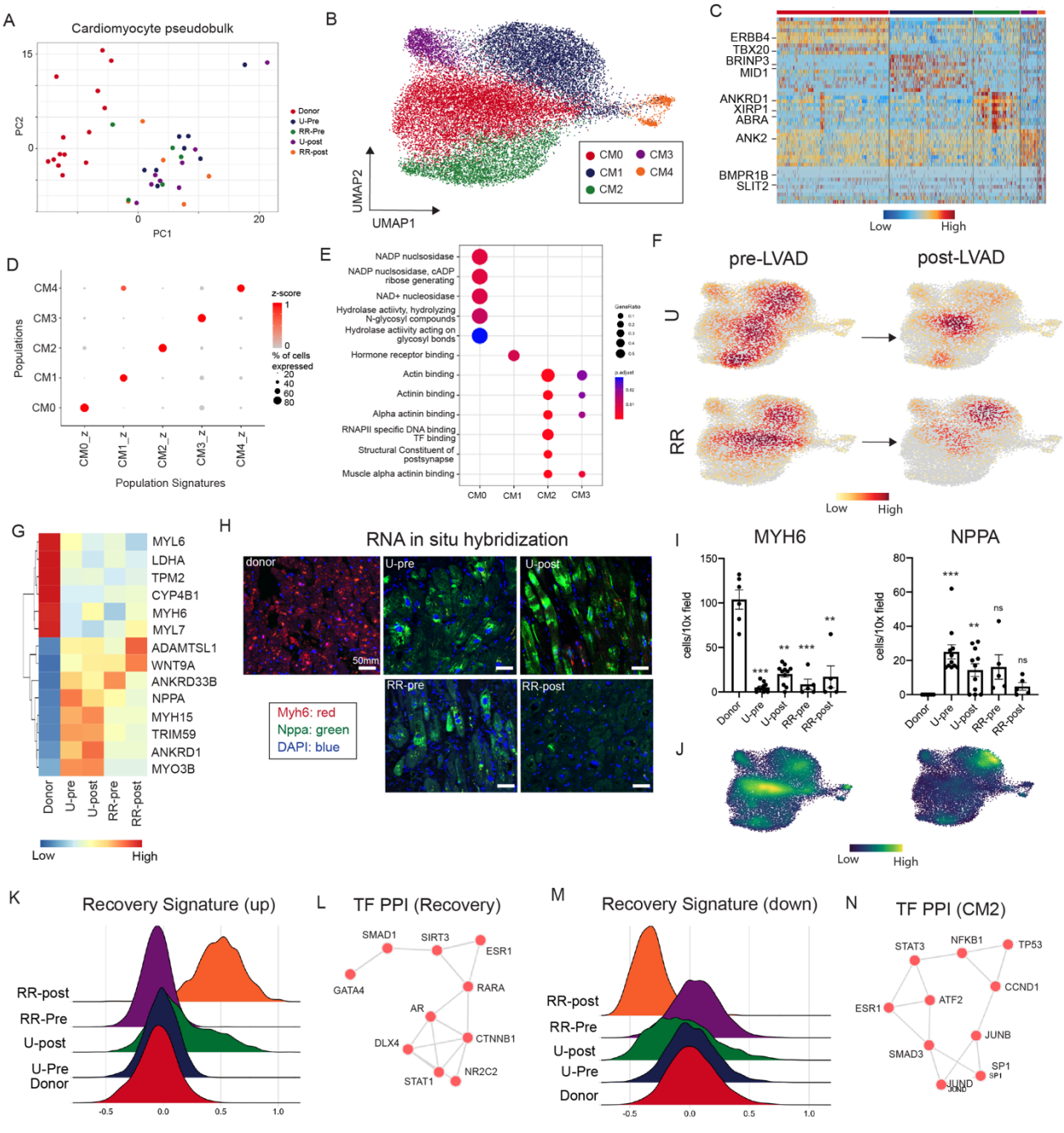
A
Cardiomyocyte pseudobulk
PC2
PC1
Donor
U-Pre
RR-Pre
U-post
RR-post
B
UMAP2
UMAP1
CM0
CM1
CM2
CM3
CM4
C
ERBB4
TBX20
BRINP3
MID1
ANKRD1
XIRP1
ABRA
ANK2
BMPR1B
SLIT2
Low
High
D
Populations
CM4
CM3
CM2
CM1
CM0
z-score
% of cells expressed
Population Signatures
E
NADP nucleosidase
NADP nucleosidase, cADP ribose generating
NAD+ nucleosidase
Hydrolase activity, hydrolyzing N-glycosyl compounds
Hydrolase activity acting on glycosyl bonds
Hormone receptor binding
Actin binding
Actinin binding
Alpha actinin binding
RNAPII specific DNA binding TF binding
Structural Constituent of postsynapse
Muscle alpha actinin binding
F
pre-LVAD
post-LVAD
U
RR
Low
High
G
MYL6
LDHA
TPM2
CYP4B1
MYH6
MYL7
ADAMTSL1
WNT9A
ANKRD33B
NPPA
MYH15
TRIM59
ANKRD1
MYO3B
Donor
U-pre
U-post
RR-pre
RR-post
Low
High
H
RNA in situ hybridization
donor
U-pre
U-post
RR-pre
RR-post
50mm
Myh6: red
Nppa: green
DAPI: blue
I
MYH6
NPPA
cells/10x field
Donor
U-pre
U-post
RR-pre
RR-post
J
Low
High
K
Recovery Signature (up)
RR-post
RR-Pre
U-post
U-Pre
Donor
L
TF PPI (Recovery)
SMAD1
SIRT3
ESR1
GATA4
RARA
AR
DLX4
CTNNB1
STAT1
NR2C2
M
Recovery Signature (down)
RR-post
RR-Pre
U-post
U-Pre
Donor
N
TF PPI (CM2)
STAT3
NFKB1
TP53
CCND1
ESR1
ATF2
JUNB
SMAD3
SP1
JUND

1105 **Figure 3.** Cardiomyocytes do not revert to a healthy state in cardiac recovery. (A) Cardiomyocyte
1106 pseudobulk PCA representation of each patient sample colored by condition. (B) UMAP
1107 embedding plot of cardiomyocytes. (C) Heatmap of marker genes for distinct cardiomyocyte cell
1108 states. (D) Dot plot of gene set z-scores for top 10 genes in each cardiomyocyte cell state. (E)
1109 Enriched GO pathways for cardiomyocyte cell states using statistically significant marker genes
1110 identified using a Wilcoxon Rank Sum test (adjusted p-value < 0.05 and log2 fold-change > 0.58).
1111 Dot size refers to gene ratio and color of dots refers to the adjusted p-value. (F) Gaussian kernel
1112 density estimation of number of nuclei in the UMAP embedding split by condition. (G) Pseudobulk
1113 heatmap of canonical genes up and down in heart failure split by condition. (H) Fluorescent
1114 RNAscope in situ hybridization for MYH6 and NPPA in donor, pre-LVAD unloaded, pre-LVAD
1115 reverse remodeled, post-LVAD unloaded and post-LVAD reverse remodeled. Images are at 10x
1116 magnification. (I) Quantification of number cells per 10x field for MYH6 and NPPA across the five
1117 conditions. Brown-Forsythe and Welch ANOVA test comparing each condition to donor. Asterisks
1118 indicate degree of statistical significance. For MYH6 n = 38 total samples and Brown-Forsythe
1119 ANOVA test F = 28.91, DFn = 4, and p < 0.0001; U-pre (***P = 0.001), U-post (**P = 0.0011), RR-
1120 pre (***P = 0.0004), and RR-post (**P = 0.0019) relative to donor. For NPPA n = 38 total samples
1121 and Brown-Forsythe ANOVA test F = 6.040, DFn = 4, and p = 0.004; U-pre (***P = 0.0001), U-
1122 post (**P = 0.0033), RR-pre (ns P = 0.086), and RR-post (ns P = 0.1017) relative to donor. (J)
1123 Density plots of MYH6 and NPPA expression in UMAP embedding. (K) Up regulated pseudobulk
1124 recovery signature Ridge plot split across five conditions. (L) Transcription factor protein-protein
1125 interactions for genes up regulated in recovery. (M) Down regulated pseudobulk recovery
1126 signature Ridge plot split across five conditions. (N) Transcription factor protein-protein
1127 interactions for CM2 marker genes downregulated in cardiac recovery.
1128
1129
1130
1131
1132
1133
1134
1135
1136
1137
1138

Figure 4

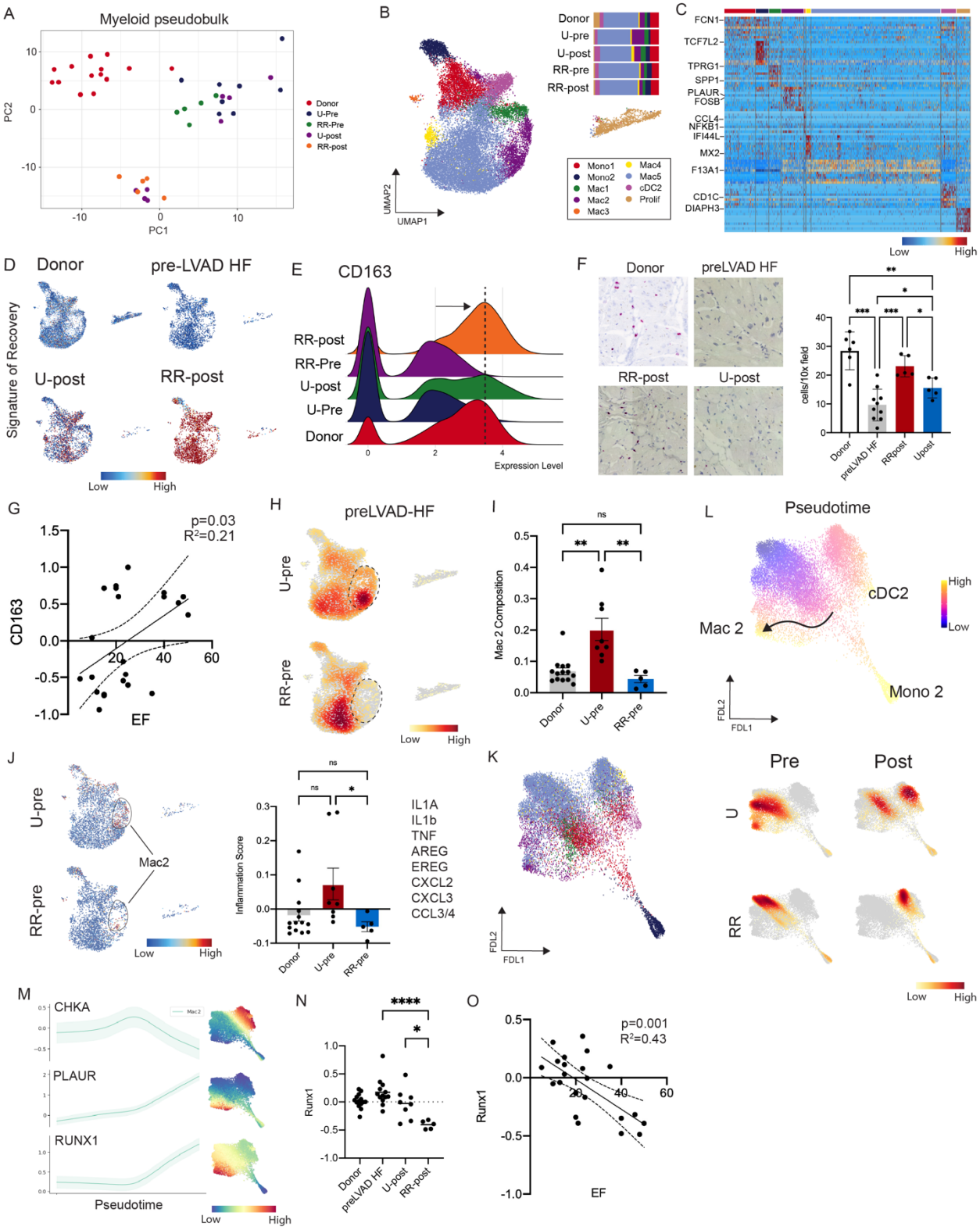
A
Myeloid pseudobulk
PC2
PC1
Donor
U-Pre
RR-Pre
U-post
RR-post
B
UMAP2
UMAP1
Donor
U-pre
U-post
RR-pre
RR-post
Mono1
Mono2
Mac1
Mac2
Mac3
Mac4
Mac5
cDC2
Prolif
C
FCN1
TCF7L2
TPRG1
SPP1
PLAUR
FOSB
CCL4
NFKB1
IFI44L
MX2
F13A1
CD1C
DIAPH3
Low
High
D
Donor
pre-LVAD HF
U-post
RR-post
Signature of Recovery
Low
High
E
CD163
RR-post
RR-Pre
U-post
U-Pre
Donor
Expression Level
F
Donor
preLVAD HF
RR-post
U-post
cells/10x field
Donor
preLVAD HF
RRpost
Upost
G
p=0.03
R²=0.21
CD163
EF
H
preLVAD-HF
U-pre
RR-pre
Low
High
I
Mac 2 Composition
Donor
U-pre
RR-pre
L
Pseudotime
cDC2
Mac 2
Mono 2
High
Low
FDL2
FDL1
J
U-pre
RR-pre
Mac2
Low
High
Inflammation Score
Donor
U-pre
RR-pre
IL1A
IL1b
TNF
AREG
EREG
CXCL2
CXCL3
CCL3/4
K
FDL2
FDL1
Pre
Post
U
RR
Low
High
M
CHKA
PLAUR
RUNX1
Pseudotime
Low
High
N
Runx1
Donor
preLVAD HF
U-post
RR-post
O
p=0.001
R²=0.43
Runx1
EF

1141 **Figure 4.** Pro-inflammatory macrophages and *RUNX1* diminished in reverse remodeling while
1142 resident macrophages show signs of recovery. (A) Myeloid pseudobulk PCA representation of
1143 each patient sample colored by condition. (B) UMAP embedding plot of myeloid cell states. (C)
1144 Heatmap of marker genes for distinct myeloid cell states. (D) Recovery up regulated signature in
1145 four conditions. (E) Ridge plot of CD163 expression split by five conditions. (F) RNAscope in situ
1146 hybridization of representative 10x fields from a donor, pre-LVAD HF, U-post, and RR-post
1147 sample (left) and quantification of number of CD163+ cells per 10x field across the four conditions
1148 (right). Brown-Forsythe and Welch ANOVA tests with multiple comparisons. Asterisks indicate
1149 degree of statistical significance. n = 26 total samples and Brown-Forsythe ANOVA test F = 20.78,
1150 DFn = 3, and p < 0.0001; donor vs preLVAD HF (***P = 0.0002), donor vs RR-post (nsP = 0.1251),
1151 donor vs U-post (**P = 0.0034), preLVAD HF vs RR-post (***P = 0.0001), preLVAD HF vs U-post
1152 (*P = 0.0256), and RR-post vs U-post (*P = 0.0108). (G) Linear regression of CD163 pseudobulk
1153 expression and patient ejection fraction in pre- and post-cohorts. Dotted line indicates 95%
1154 confidence interval, R^2 goodness of fit, and p-value indicating whether the slope is significantly
1155 non-zero using an F test. (H) Gaussian kernel density estimation of cells in unloaded pre-LVAD
1156 and reverse remodeled pre-LVAD. (I) Mac2 cell state composition in donors and pre-LVAD
1157 patients. Dunn's multiple comparisons test: donor vs U-pre (**P = 0.0045), U-pre vs RR-pre (**P
1158 = 0.0041), and donor vs RR-pre (nsP > 0.9999). (J) Gene set z-score for inflammation in unloaded
1159 pre-LVAD and reverse remodeled pre-LVAD (left) and quantified at patient level (right). Un-paired
1160 t-test with Welch's correction: U-pre vs RR-pre (*P = 0.0321), donor vs U-pre (nsP = 0.1006), and
1161 donor vs RR-pre (nsP = 0.1602). (K) FDL embedding plot of myeloid cell states with colors from
1162 (B). (L) Palantir derived pseudotime in a FDL embedding plot with terminal states (Mac1, cDC2,
1163 and Mono2) using classical monocytes as a start state (top) and Gaussian density plot of cell
1164 number in FDL embedding split by four conditions (bottom). (M) CHKA, PLAUR, and RUNX1 gene
1165 expression along pseudotime (left) and expression in FDL embedding space (right). (N)
1166 Pseudobulk RUNX1 expression in pre-LVAD HF, U-post, and RR-post. Un-paired t-test with
1167 Welch's correction: pre-LVAD HF vs U-post (nsP = 0.1177), pre-LVAD HF vs RR-post (****P <
1168 0.0001), and U-post vs RR-post (**P = 0.0058). (O) Linear regression of RUNX1 pseudobulk
1169 expression and patient ejection fraction in pre- and post-cohorts. Dotted line indicates 95%
1170 confidence interval, R^2 goodness of fit, and p-value indicating whether the slope is significantly
1171 non-zero using an F test.
1172
1173
1174

Figure 5

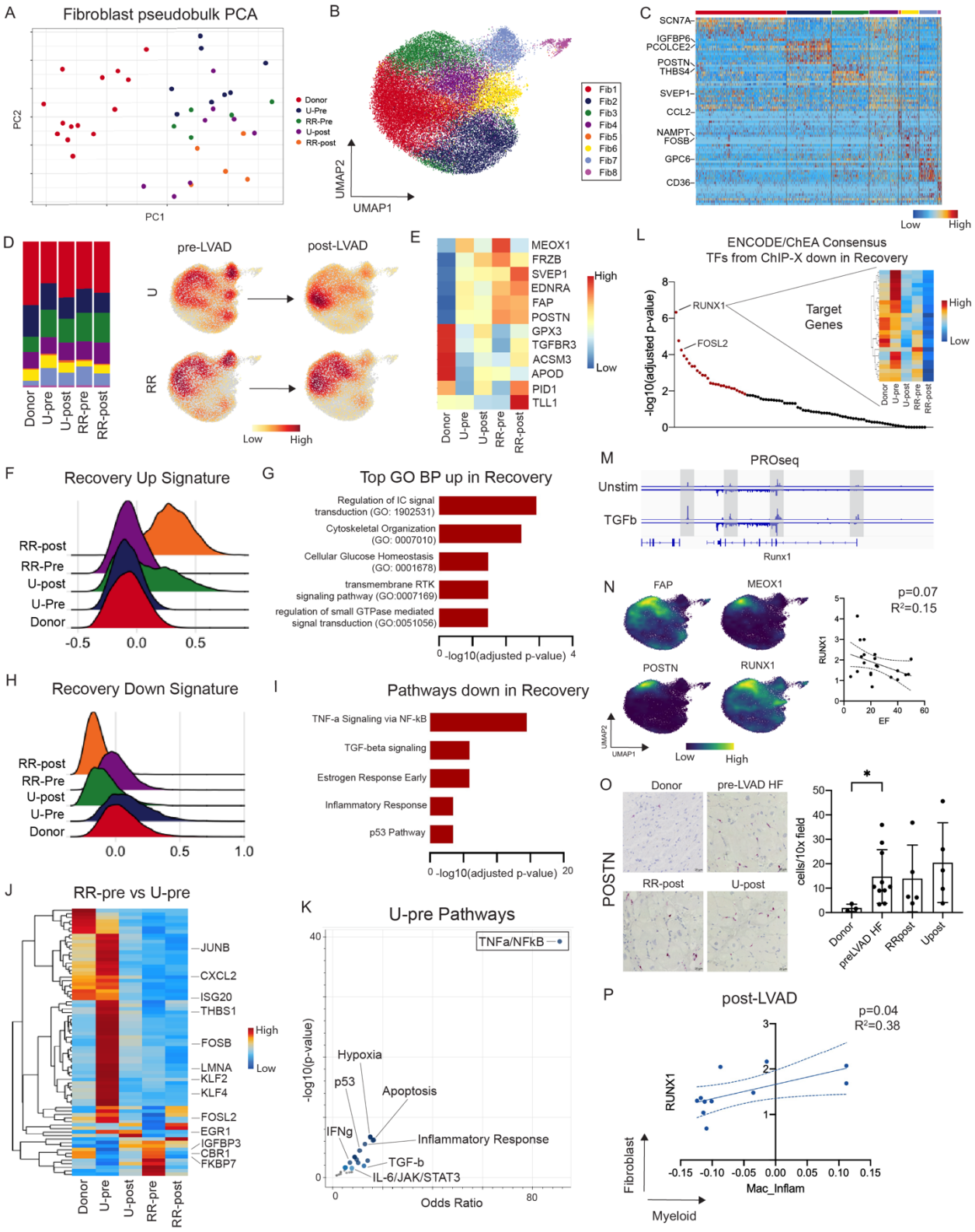
A
Fibroblast pseudobulk PCA
PC2
PC1
Donor
U-Pre
RR-Pre
U-post
RR-post
B
UMAP2
UMAP1
Fib1
Fib2
Fib3
Fib4
Fib5
Fib6
Fib7
Fib8
C
SCN7A
IGFBP6
PCOLCE2
POSTN
THBS4
SVEP1
CCL2
NAMPT
FOSB
GPC6
CD36
Low
High
D
Donor
U-pre
U-post
RR-pre
RR-post
pre-LVAD
post-LVAD
U
RR
Low
High
E
MEOX1
FRZB
SVEP1
EDNRA
FAP
POSTN
GPX3
TGFBR3
ACSM3
APOD
PID1
TLL1
High
Low
L
ENCODE/ChEA Consensus
TFs from ChIP-X down in Recovery
-log10(adjusted p-value)
RUNX1
FOSL2
Target
Genes
High
Low
F
Recovery Up Signature
RR-post
RR-Pre
U-post
U-Pre
Donor
-0.5
0.0
0.5
G
Top GO BP up in Recovery
Regulation of IC signal transduction (GO: 1902531)
Cytoskeletal Organization (GO: 0007010)
Cellular Glucose Homeostasis (GO: 0001678)
transmembrane RTK signaling pathway (GO:0007169)
regulation of small GTPase mediated signal transduction (GO:0051056)
-log10(adjusted p-value)
M
PROseq
Unstim
TGFb
Runx1
H
Recovery Down Signature
RR-post
RR-Pre
U-post
U-Pre
Donor
0.0
0.5
1.0
I
Pathways down in Recovery
TNF-a Signaling via NF-kB
TGF-beta signaling
Estrogen Response Early
Inflammatory Response
p53 Pathway
-log10(adjusted p-value)
N
FAP
MEOX1
POSTN
RUNX1
UMAP2
UMAP1
Low
High
p=0.07
R²=0.15
RUNX1
EF
O
Donor
pre-LVAD HF
RR-post
U-post
POSTN
cells/10x field
Donor
preLVAD HF
RRpost
Upost
J
RR-pre vs U-pre
JUNB
CXCL2
ISG20
THBS1
FOSB
LMNA
KLF2
KLF4
FOSL2
EGR1
IGFBP3
CBR1
FKBP7
High
Low
Donor
U-pre
U-post
RR-pre
RR-post
K
U-pre Pathways
TNFa/NFkB
-log10(p-value)
Hypoxia
p53
Apoptosis
IFNg
Inflammatory Response
TGF-b
IL-6/JAK/STAT3
Odds Ratio
P
post-LVAD
p=0.04
R²=0.38
RUNX1
Fibroblast
Myeloid
Mac_Inflam

1177 **Figure 5**. RUNX1 is downregulated in fibroblasts in cardiac recovery. (A) Fibroblast pseudobulk
1178 principle component analysis representation of each patient sample colored by condition. (B)
1179 UMAP embedding plot of fibroblast cell states. (C) Heatmap of marker genes for distinct fibroblast
1180 cell states. (D) Cell composition of fibroblast cell states across five conditions (left) and Gaussian
1181 kernel density estimation of cells in four conditions pre- and post-LVAD implantation (right). (E)
1182 Heatmap of expression of canonical genes up and downregulated in fibroblasts in heart failure
1183 across five conditions. (F) Up and (H) down regulated pseudobulk recovery signature Ridge plot
1184 split across five conditions. (G) GO biological processes pathways enriched in recovery and (I)
1185 pathways down in recovery. (J) Heatmap of pseudobulk DE analysis between RR-pre and U-pre
1186 split across 5 conditions. (K) Volcano Plot of pathways enriched in unloaded group pre-LVAD
1187 implantation where each point is a gene set pathway, and the color of the points represents
1188 degree of statistical significance. (L) Transcription factors down in cardiac recovery from
1189 ENCODE/ChEA consensus; x-axis is transcription factors and red dots are TFs which are
1190 statistically significant. Heatmap showing expression of RUNX1 target genes across five
1191 conditions. (M) PRO-seq coverage in unstimulated and TGF-b treated *in vitro* fibroblasts
1192 (GSE15582) at the *RUNX1* locus. (N) Density plots of HF genes in UMAP embedding (left) and
1193 linear regression of RUNX1 pseudobulk expression and patient ejection fraction in pre- and post-
1194 cohorts (right). Dotted line indicates 95% confidence interval, R^2 goodness of fit, and p-value
1195 indicating whether the slope is significantly non-zero using an F test. (O) RNAscope in situ
1196 hybridization of representative 10x fields from a donor, pre-LVAD HF, U-post, and RR-post
1197 sample (left) and quantification of number of POSTN+ cells per 10x field across the four conditions
1198 (right). Brown-Forsythe and Welch ANOVA tests with multiple comparisons. Asterisks indicate
1199 degree of statistical significance. Donor vs pre-LVAD HF (*P = 0.0272). (P) Linear regression of
1200 RUNX1 pseudobulk expression in fibroblasts and inflammatory signature in macrophages in post-
1201 LVAD cohort. Dotted line indicates 95% confidence interval, R^2 goodness of fit, and p-value
1202 indicating whether the slope is significantly non-zero using an F test.
1203
1204
1205
1206
1207
1208
1209
1210

Figure 6

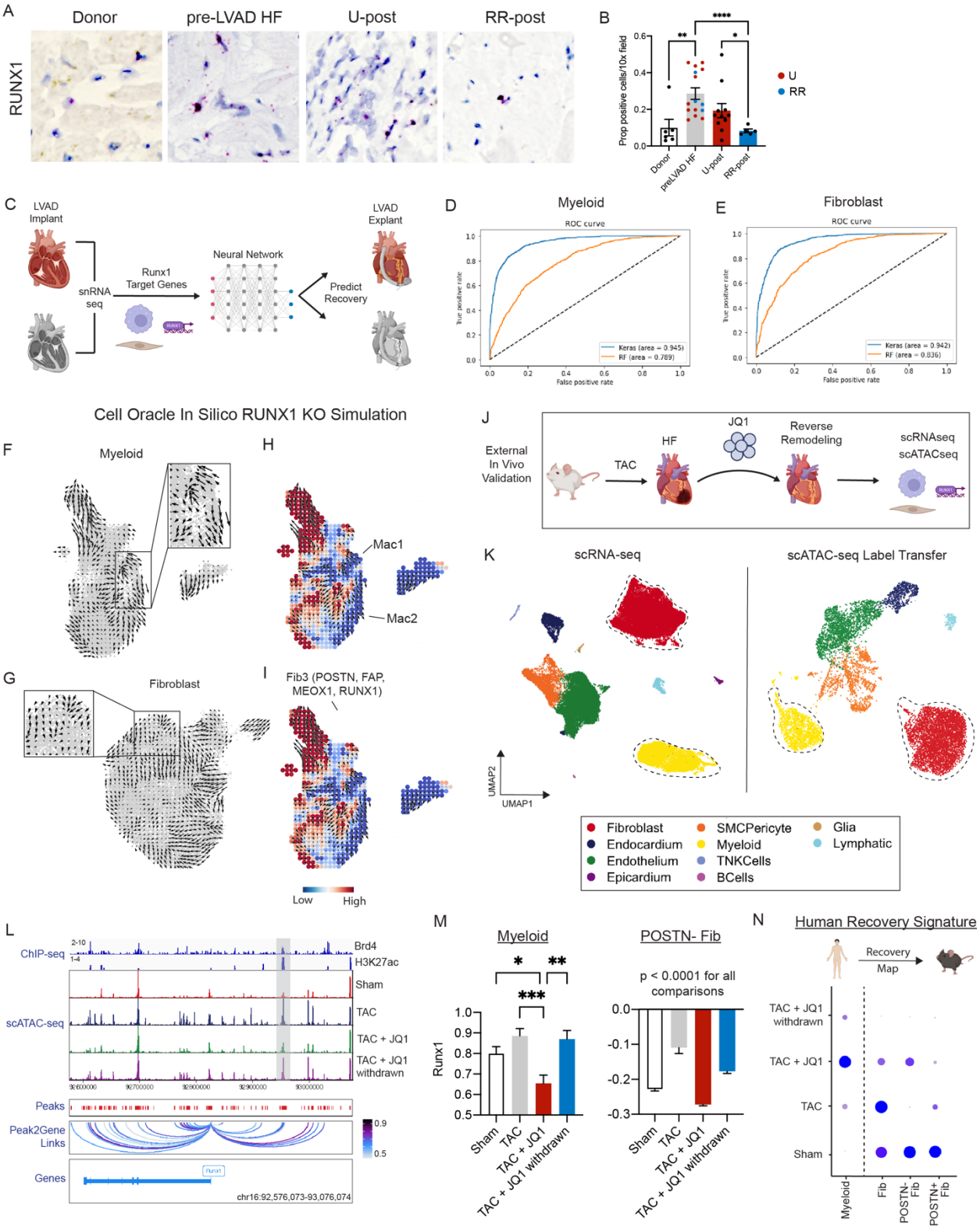
A
Donor
pre-LVAD HF
U-post
RR-post
RUNX1
B
Prop positive cells/10x field
Donor
preLVAD HF
U-post
RR-post
U
RR
C
LVAD Implant
snRNA seq
Runx1 Target Genes
Neural Network
Predict Recovery
LVAD Explant
D
Myeloid
ROC curve
Keras (area = 0.945)
RF (area = 0.789)
E
Fibroblast
ROC curve
Keras (area = 0.942)
RF (area = 0.836)
Cell Oracle In Silico RUNX1 KO Simulation
F
Myeloid
H
Mac1
Mac2
G
Fibroblast
I
Fib3 (POSTN, FAP, MEOX1, RUNX1)
Low
High
J
External In Vivo Validation
TAC
HF
JQ1
Reverse Remodeling
scRNAseq
scATACseq
K
scRNA-seq
scATAC-seq Label Transfer
UMAP2
UMAP1
Fibroblast
Endocardium
Endothelium
Epicardium
SMCPericyte
Myeloid
TNKCells
BCells
Glia
Lymphatic
L
ChIP-seq
Brd4
H3K27ac
scATAC-seq
Sham
TAC
TAC + JQ1
TAC + JQ1 withdrawn
Peaks
Peak2Gene Links
Genes
chr16:92,576,073-93,076,074
M
Myeloid
POSTN- Fib
p < 0.0001 for all comparisons
Runx1
Sham
TAC
TAC + JQ1
TAC + JQ1 withdrawn
N
Human Recovery Signature
Recovery Map
TAC + JQ1 withdrawn
TAC + JQ1
TAC
Sham
Myeloid
Fib
POSTN- Fib
POSTN+ Fib

1213 **Figure 6.** *RUNX1* perturbation *in silico* and *in vivo* facilitates cardiac recovery. (A) RNAscope in
1214 situ hybridization for Runx1 in a representative donor, pre-LVAD HF sample, U-post, and RR-
1215 post. (B) RNAscope images quantified as proportion of positive interstitial nuclei/total interstitial
1216 nuclei per 10x field. Brown-Forsythe and Welch ANOVA test comparing each condition to donor.
1217 Asterisks indicate degree of statistical significance. n = 37 total samples and Brown-Forsythe
1218 ANOVA test F = 7.686, DFn = 3, and p = 0.0009. Asterisks indicate degree of statistical
1219 significance: *P < 0.05, **P < 0.01, and ***P < 0.001. p-value specified for non-significant
1220 comparison. (C) Schematic of machine learning approach used to predict recovery in
1221 macrophages and fibroblasts with Runx1 target genes as features. ROC curves with accuracy
1222 metrics for test dataset in predicting recovery in (D) macrophages and (E) fibroblasts using a
1223 Keras deep neural net classifier model and random forest classifier. CellOracle in silico Runx1
1224 KO simulation quiver plot of vector field in (F) macrophages and (G) fibroblasts. Perturbation
1225 score with vector field in (H) macrophages and (I) fibroblasts. (J) Study design of external
1226 validation dataset. (K) scRNA-seq and scATAC-seq UMAP embedding with cell labels from RNA-
1227 seq label transferred onto ATAC-seq dataset using publicly available data (GSE15582). (L)
1228 Mouse *Runx1* locus showing from top to bottom: ChIP-seq for BRD4 (GSE46668) and H3K27ac
1229 (ENCSR000CDF) in adult mouse heart and scATAC-seq in mouse fibroblasts split by four
1230 conditions with called peaks (GSE15582), and peak2gene links from ArchR. Numbers above tract
1231 indicate ranges of normalized tag densities. Highlighted area is a peak linked to the Runx1 gene.
1232 (M) *Runx1* expression in macrophages (left) and *Postn*- fibroblasts (right) in Sham, TAC, TAC +
1233 JQ1, and TAC + JQ1 withdrawn. Brown-Forsythe and Welch ANOVA multiple comparisons test.
1234 Myeloid: Sham vs TAC + JQ1 withdrawm (*P = 0.0492), TAC vs TAC + JQ1 (***P = 0.0003), and
1235 TAC + JQ1 vs TAC + JQ1 withdrawn (**P = 0.0021). Fibroblast: ****P < 0.0001 for all pairwise
1236 comparisons. (N) Dotplot of Human myeloid and fibroblast cardiac recovery gene signature
1237 plotted in mouse macrophages in fibroblasts split by 4 conditions.
1238

Extended Data Figure 1

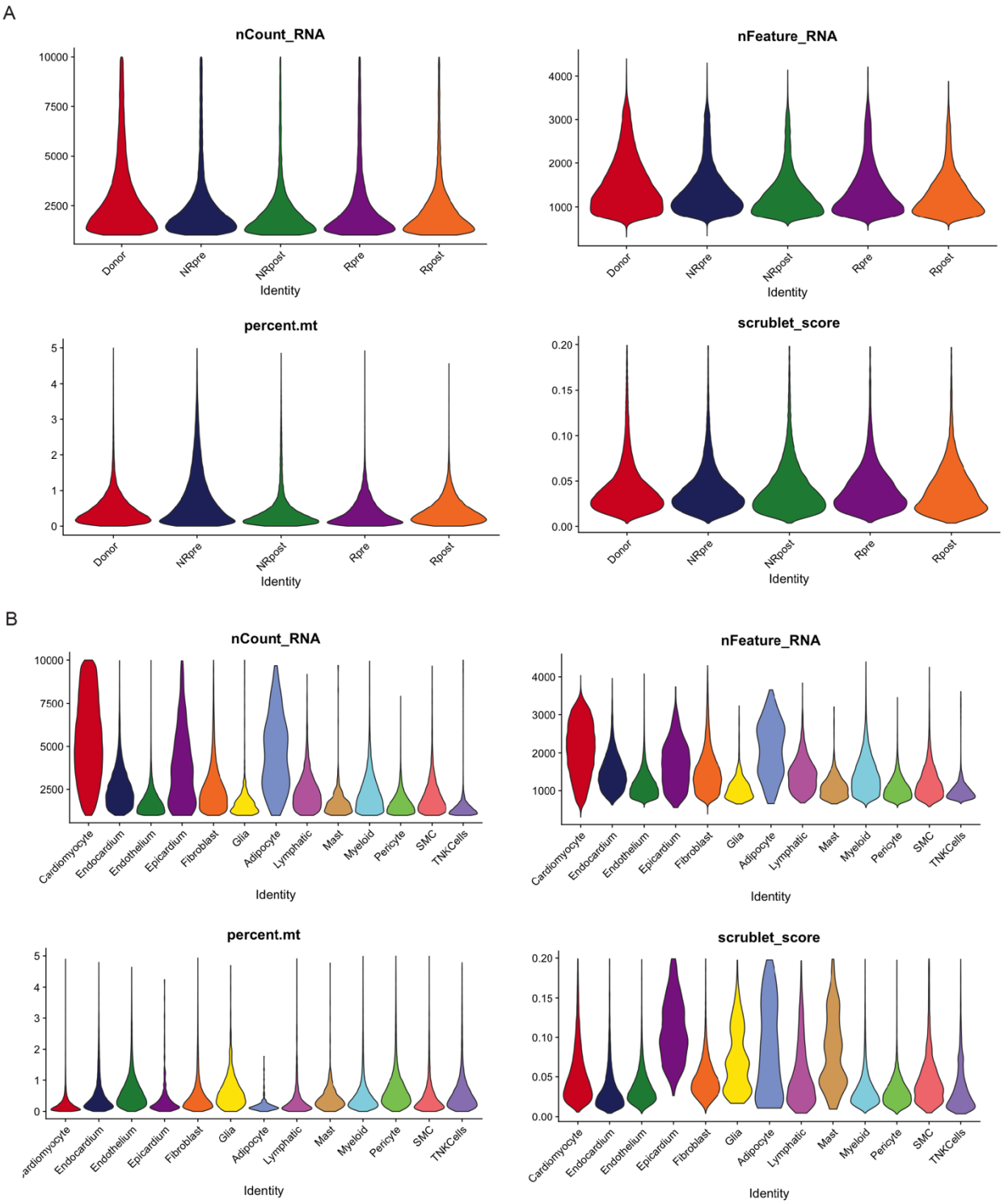

Extended Data Figure 1. Quality control metrics. nCount_RNA, nFeature_RNA, percent.mt, and scrublet doublet score split by (A) condition and (B) cell type.

Extended Data Figure 2

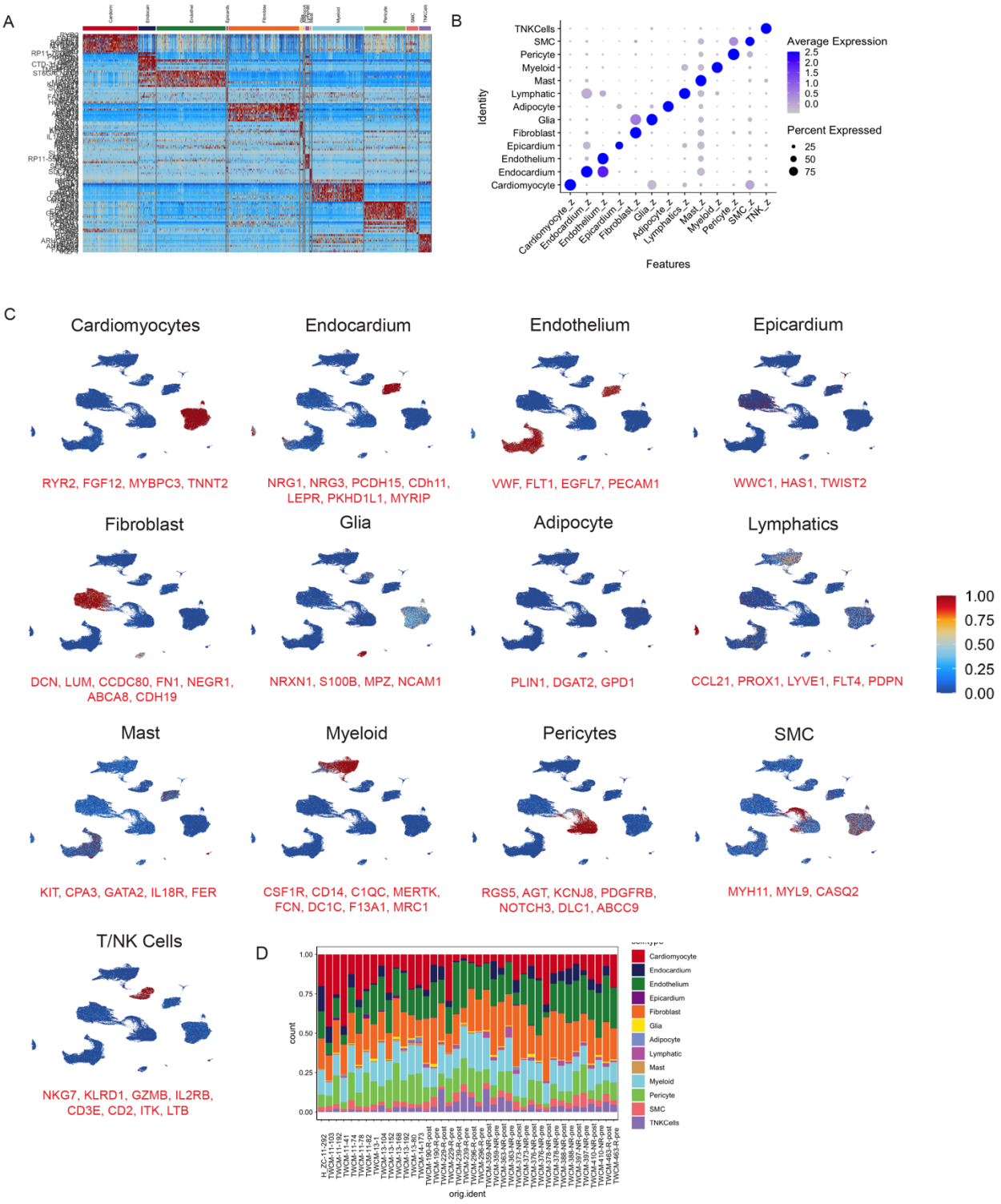

Extended Data Figure 2. Global clustering. (A) Heatmap of top10 marker gens for each cell type identified via DE analysis. (B) DotPlot for cell type gene set scores from (A) where the x-axis is cell type gene signature and y-axis is the cluster. (C) Gene set z-scores for top gene markers for each cell type plotted in the UMAP embedding. (D) Cell type composition for each of the patient samples.

Extended Data Figure 3

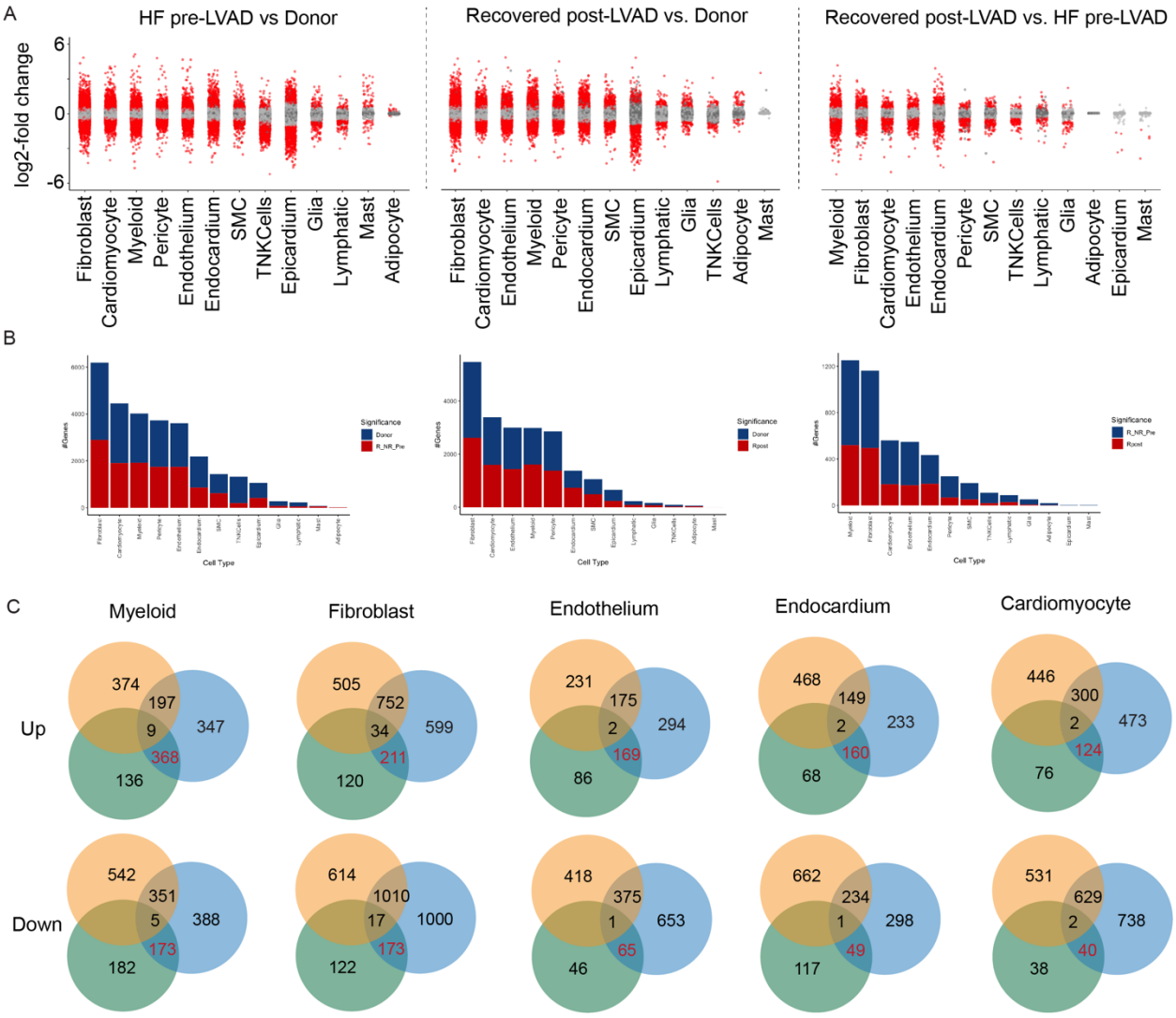

Extended Data Figure 3. Pseudobulk DE analysis to unravel cardiac recovery. (A) Pseudobulk DE analysis in each cell type in 3 comparison groups: pre-LVAD HF vs donor, RR-post vs donor, and RR-post vs pre-LVAD HF. Red dots indicate statistically significant genes (adjusted p-value < 0.05). (B) Total number of statistically significant (adjusted p-value < 0.05 and log2FC > 0.58) per cell type in comparisons from (A). (C) Number of overlapping genes in five major cell populations which are up and down in the comparisons from (A). Red number is the number of cardiac recovery genes.

Extended Data Figure 4

A

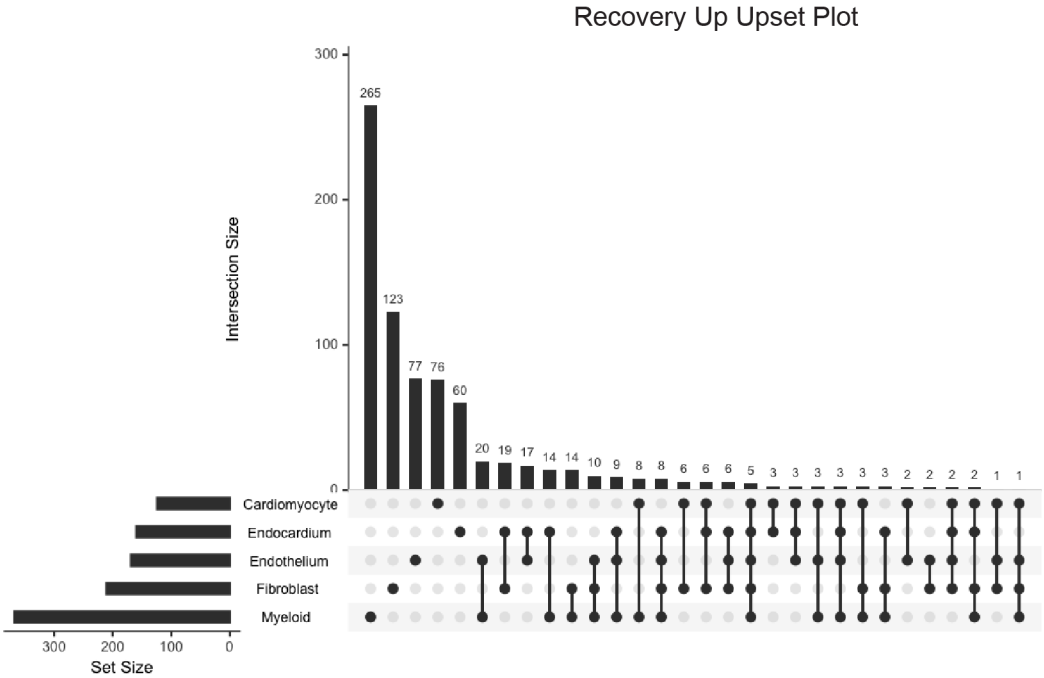

B

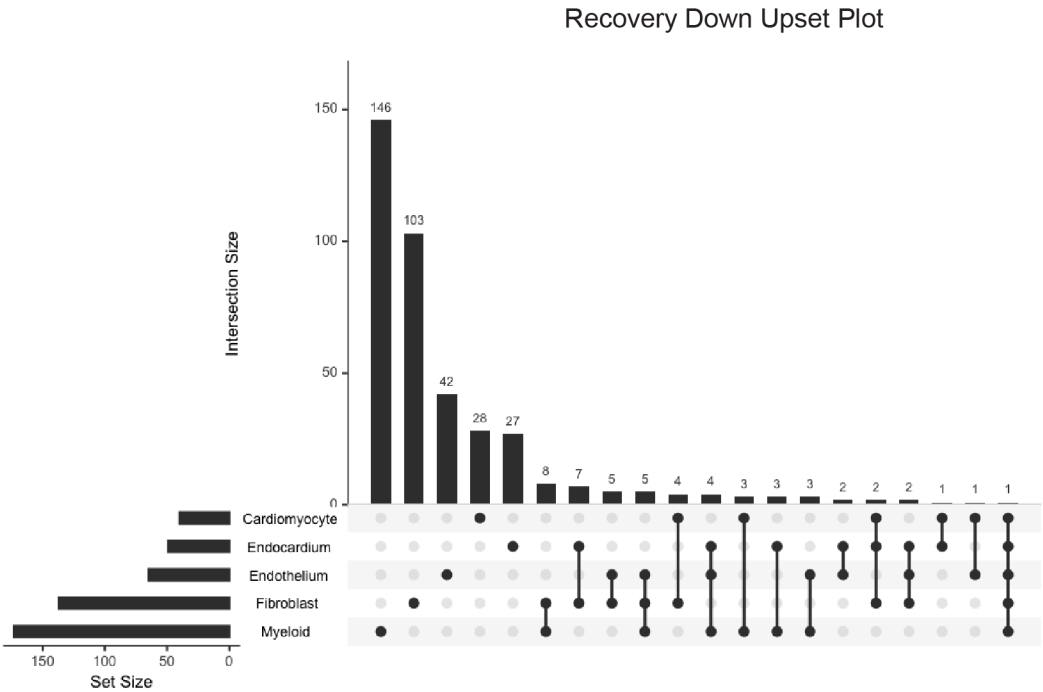

Extended Data Figure 4. Cardiac recovery overlap amongst cell types. UpSet plot showing overlap in cardiac recovery genes from (Fig.2) in five major cell populations which are (A) up and (B) down in cardiac recovery.

Extended Data Figure 5

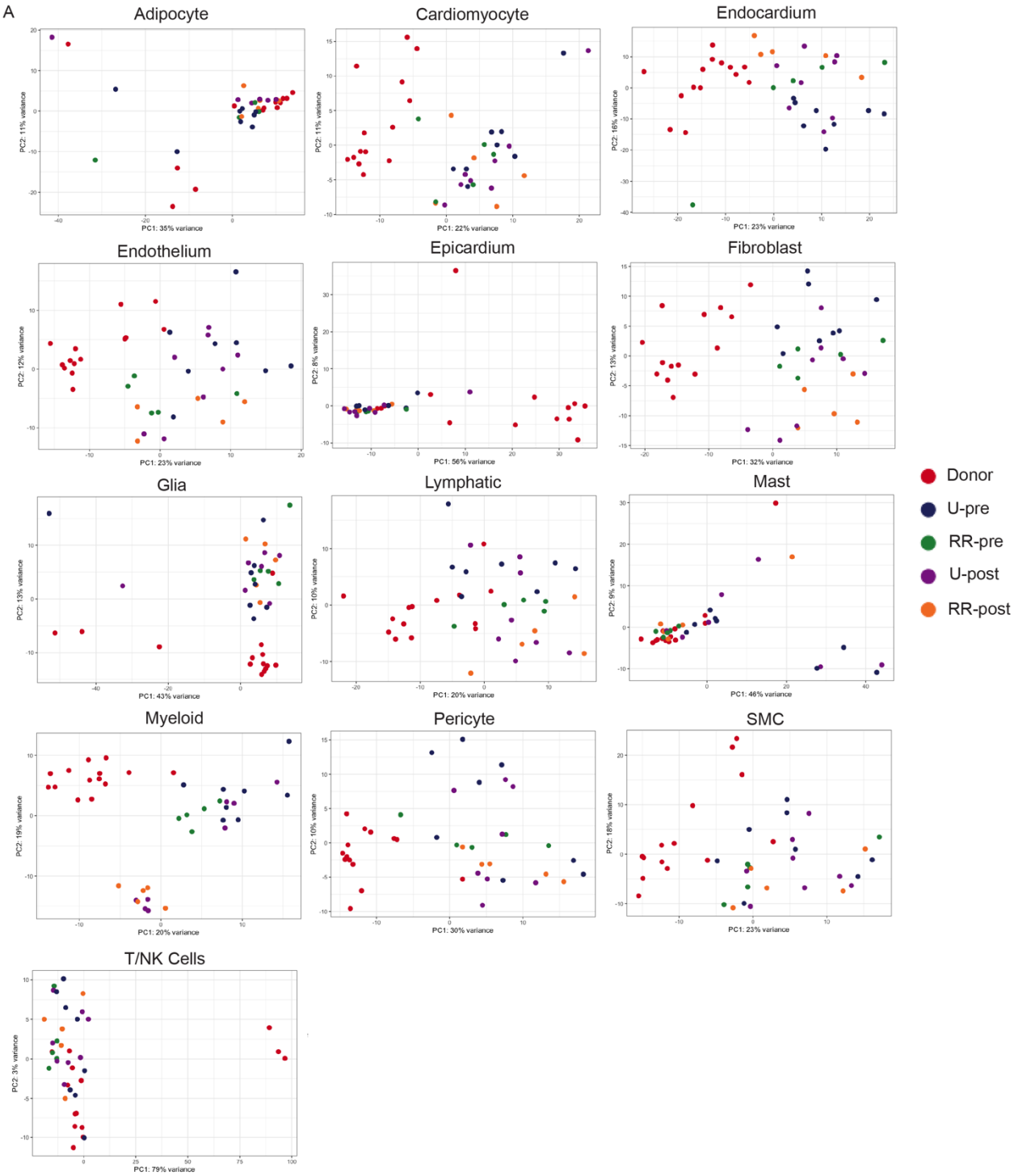

Extended Data Figure 5. Pseudobulk PCA analysis in each cell type colored by five conditions (donor, U-pre, U-post, RR-pre, and RR-post).

Extended Data Figure 6

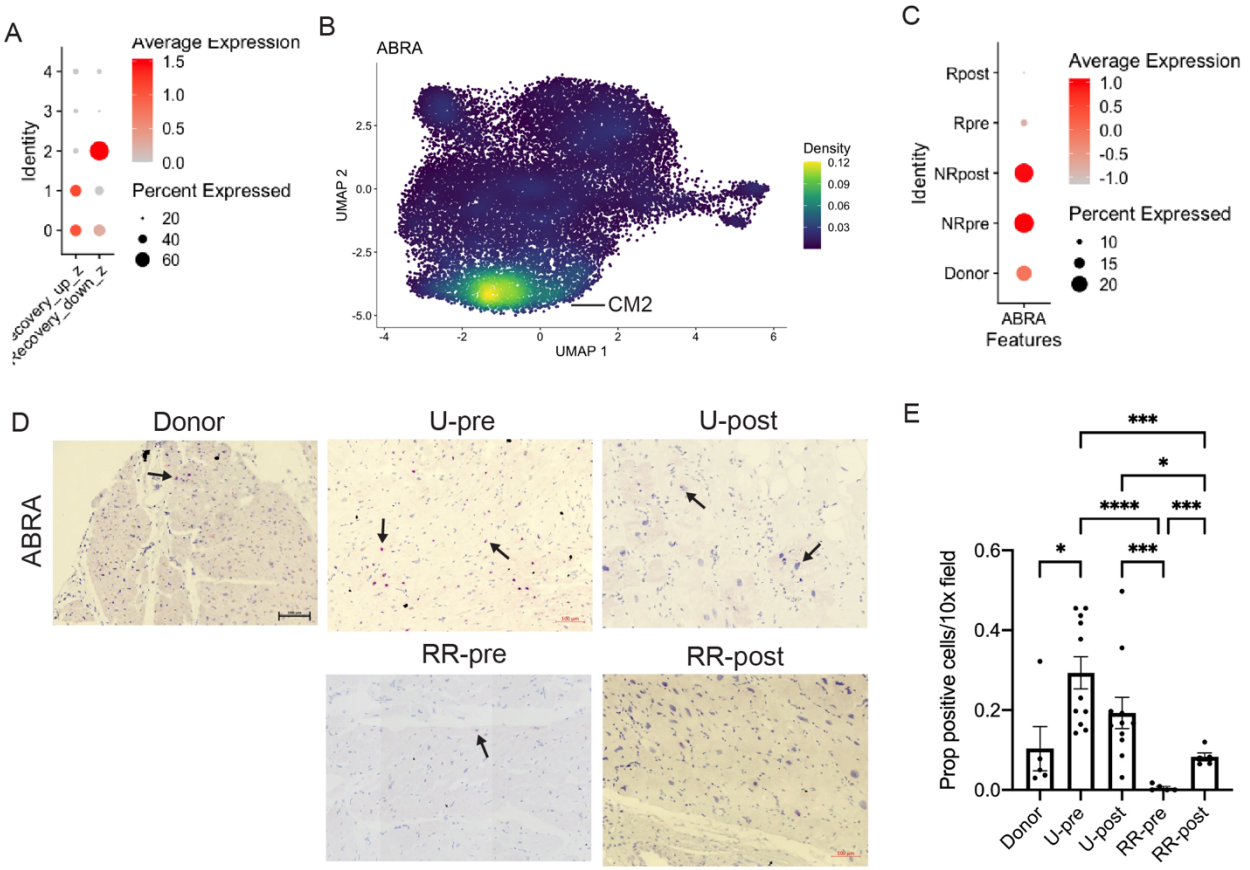

Extended Data Figure 6. ABRA expression enriched in unloaded group. (A) DotPlot of cardiomyocyte specific recovery up- and down signature grouped by CM cell states. (B) Density plot of ABRA expression in UMAP embedding. (C) DotPlot of ABRA expression in cardiomyocytes grouped by condition. (D) RNAscope images of ABRA in 5 conditions. (E) RNAscope images quantified across an array of patients. Un-paired t-test with Welch's correction used for comparisons; donor vs U-pre (*P = 0.023), U-pre vs RR-pre (***P < 0.0001), U-pre vs RR-post (***P = 0.0003), U-post vs RR-pre (***P = 0.0007), U-post vs RR-post (*P = 0.0188), and RR-pre vs RR-post (***P = 0.0007).

Extended Data Figure 7

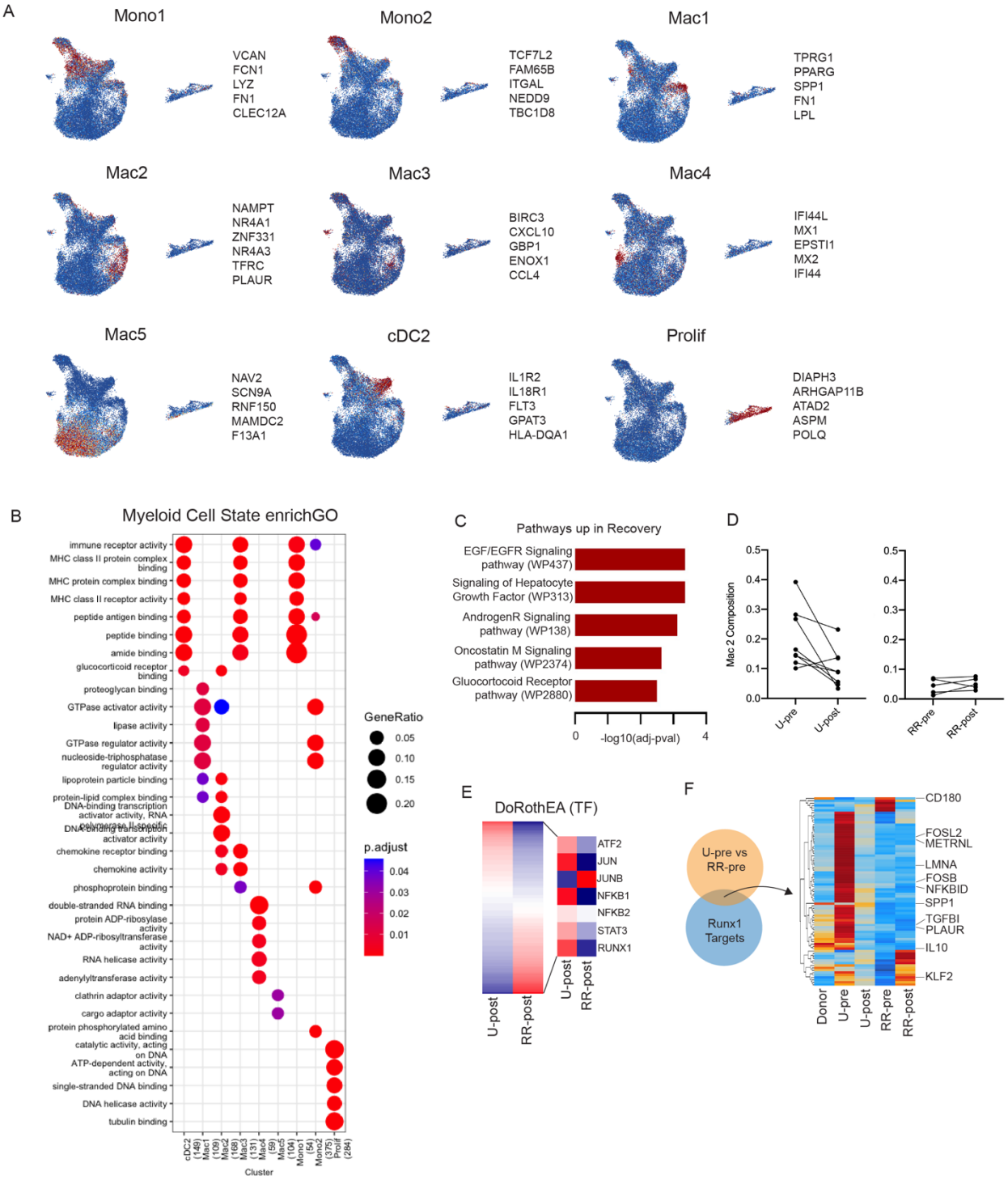

Extended Data Figure 7. Macrophage diversity in recovery. (A) Gene set z-scores for top gene markers for each cell state plotted in the UMAP embedding. (B) Enrich GO using compareclusters from cluster Prolifer across macrophage cell states. (C) WikiPathways enriched in cardiac recovery. (D) Paired comparison of Mac 2 cluster composition at patient level split by U and RR group. (E) DoRothEA TF enrichment analysis in U-post and RR-post zoomed in on some key differentially enriched TFs. (F) Overlap between Runx1 target genes and DE genes between U-pre and RR-pre with heatmap of respective genes split by condition.

Extended Data Figure 8

A

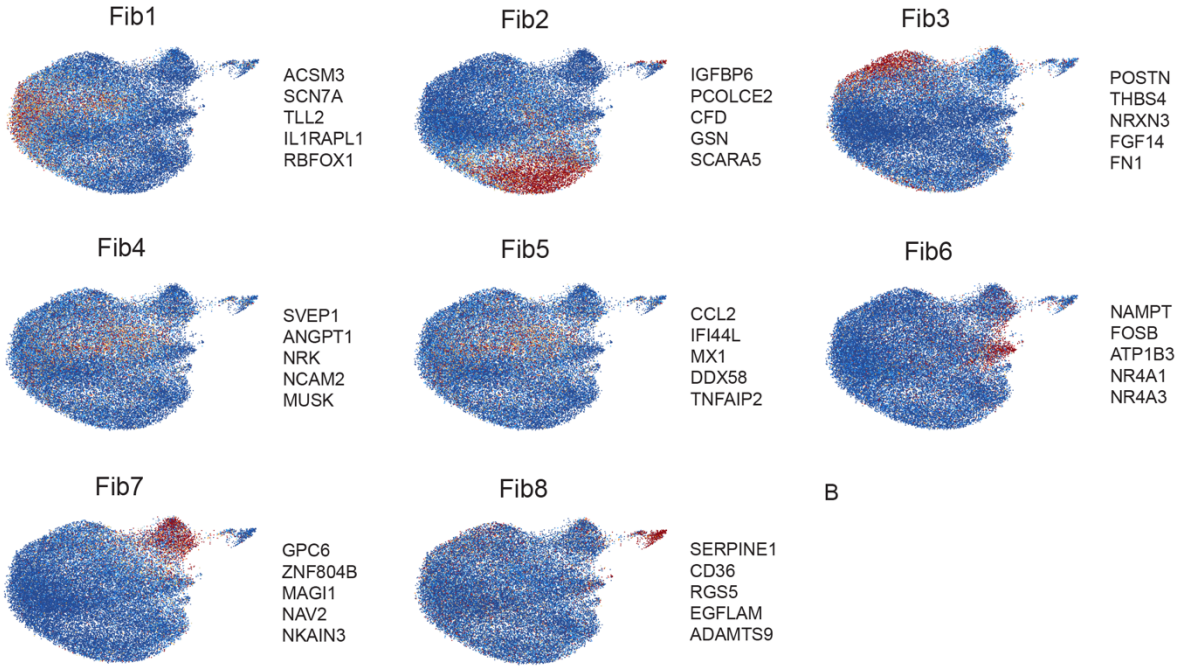

B

C

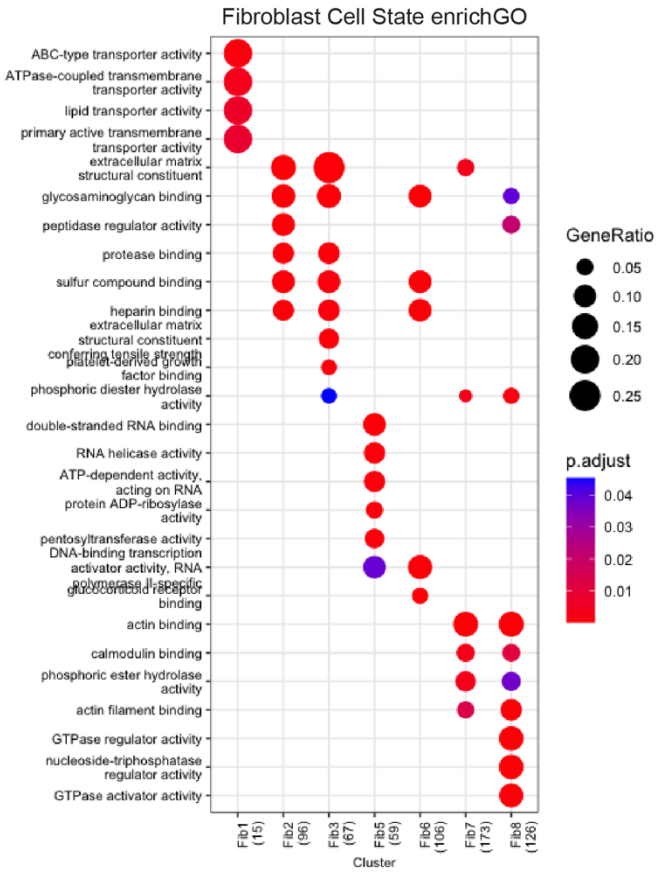

Extended Data Figure 8. Fibroblast diversity in recovery. (A) Gene set z-scores for top gene markers for each cell state plotted in the UMAP embedding. (B) DotPlot for cell type gene set scores from (A) where the x-axis is cell type gene signature and y-axis is the cluster. (C) Enrich GO using compareclusters from cluster Prolifer across fibroblast cell states.

Extended Data Figure 9

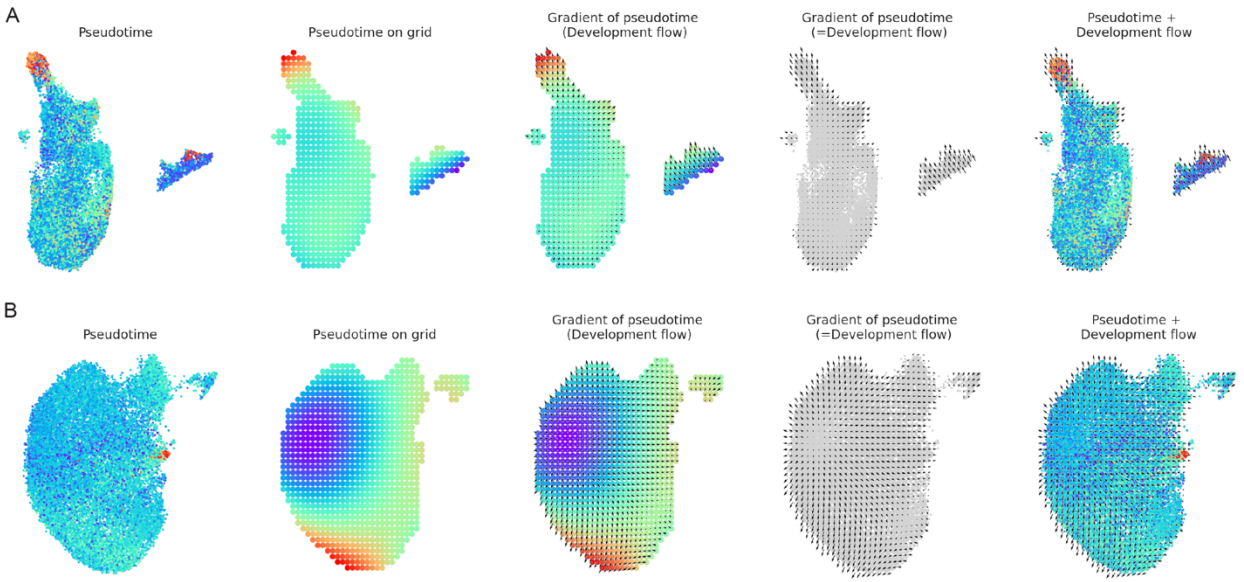

1545 **Extended Data Figure 9.** CellOracle developmental flow and digitized grid construction in (A)
1546 Macrophages and (B) Fibroblasts.